

Continuum theory of partially fluidized granular flows

Igor S. Aranson¹ and Lev S. Tsimring²

¹Argonne National Laboratory, 9700 South Cass Avenue, Argonne, Illinois 60439

²Institute for Nonlinear Science, University of California, San Diego, La Jolla, California 92093-0402

(Received 19 September 2001; revised manuscript received 18 January 2002; published 21 June 2002)

A continuum theory of partially fluidized granular flows is developed. The theory is based on a combination of the equations for the flow velocity and shear stresses coupled with the order-parameter equation which describes the transition between the flowing and static components of the granular system. We apply this theory to several important granular problems: avalanche flow in deep and shallow inclined layers, rotating drums, and shear granular flows between two plates. We carry out quantitative comparisons between the theory and experiment.

DOI: 10.1103/PhysRevE.65.061303

PACS number(s): 45.70.Mg, 47.54.+r, 47.35.+i

I. INTRODUCTION

The dynamics of granular materials under shear stresses plays a fundamental role in many natural phenomena and technological applications [1–4]. When the shear stress exceeds a certain threshold, granular material undergoes a transition from a solid state to a fluidized state (yield). The physical mechanism and properties of this transition are still not completely understood. In many important situations the granular material remains in a multiphase state when part of it is fluidized while another part is solid.

On the theoretical side, a significant progress has been achieved by large-scale molecular dynamics simulations [5,6] and by continuum theory [7–12]. The current continuum theory of dense near-surface flows was pioneered by Bouchaud, Cates, Ravi Prakash, and Edwards (BCRE) [9] and subsequently developed by de Gennes and co-workers [7,10,11]. In their model, a granular system is spatially separated into two phases, static and rolling. The interaction between the phases is implemented through certain conversion rates. This model describes certain features of thin near-surface granular flows including avalanches. However, due to its intrinsic assumptions, it only works when the granular material is well separated into a thin surface flow and an immobile bulk. In many practically important situations, this distinction between the “liquid” and “solid” phases is more subtle and itself is controlled by the dynamics.

The purpose of this paper is to develop a unifying description of such partially fluidized granular flows and apply this theory to several problems of granular dynamics [13]. The underlying idea of our approach is borrowed from the Landau theory of phase transitions [14]. We assume that the shear stresses in a partially fluidized granular matter are composed of two parts: the dynamic part proportional to the shear strain rate and the strain-independent (or “static”) part. The relative magnitude of the static shear stress is controlled by the order parameter (OP), which varies from 0 in the liquid phase to 1 in the solid phase. A possibility of describing a granular flow as a multiphase system undergoing a phase transition has been proposed by de Gennes [7] without further elaboration. Unlike ordinary matter, the phase transition in granular matter is controlled not by the temperature, but by the dynamics stresses themselves. In particular, the

Mohr-Coloumb yield failure condition [4] is equivalent to the critical melting temperature of a solid. The OP can be related to the local entropy (and possibly density) [15] of the granular material. OP dynamics is then coupled to the hydrodynamic equation for the granular flow.

We apply this theory to several cases of granular flows of considerable interest. First, we will focus on gravity driven free-surface granular flows which typically occur in shallow chutes, sandpiles, and rotating drums. The most famous form of such flows is an avalanche, and our theory yields a rather detailed description of the avalanche dynamics. Then we apply our theory to granular Couette flows induced in the bulk by a moving boundary. Our model captures important phenomenology observed in these systems [16–28].

The structure of the paper is as follows. In Sec. II we describe a general formulation of the partially fluidized granular flows. In Sec. III we focus on the free-surface flow problem on an incline plane (chute flow). In this section we consider stability properties of stationary solutions, avalanches in shallow chutes, transitions from triangular to uphill avalanches, and comparison with experimental results. In Sec. IV we study flows in deep layers. First, we consider avalanches in deep chutes. Then, we apply our theory to granular flows in two-dimensional rotating drums. We show that our model exhibits avalanche flow at low rotation rates and transition to steady flow at higher rotation rates. In Sec. V we extend our approach to shear granular flows and discuss its connection with dry friction phenomena in granular systems. In Sec. VI we discuss various implications of our results.

II. GENERAL FORMULATION

We base the continuum description of granular flows on the momentum conservation equation

$$\rho_0 \frac{Dv_i}{Dt} = \frac{\partial \sigma_{ij}}{\partial x_j} + \rho_0 g_i, \quad j=1,2,3, \quad (1)$$

where v_i are the components of velocity, $\rho_0 = \text{const}$ is the density of material (we set $\rho_0 = 1$), \mathbf{g} is acceleration of gravity, $D/Dt = \partial_t + v_i \partial_{x_i}$ denotes the material derivative, and σ_{ij} denotes components of the stress tensor. We assume that the

velocity obeys the incompressibility condition $\nabla \cdot \mathbf{v} = 0$. Indeed, the relative changes of density for dense flows are typically very small (of the order of a few percent), and therefore the compressibility is negligible in the momentum dynamics. Still, these changes in density in fact are very important, since the very onset of flow in granular materials itself is related to dilatancy, i.e., small decrease in density. Furthermore, these small variations in density substantially influence transport coefficients and the constitutive relations. In fact, our order-parameter equation (see below) is a phenomenological way to describe the small but important changes in local ordering, and, consequently, density.

The momentum conservation equation (1) has to be augmented by the appropriate boundary conditions (BCs). As usual, on solid walls we require no-slip conditions $v_i = 0$, and on free surfaces, the kinematic boundary condition is assumed,

$$\frac{D\xi}{Dt} = v_n, \quad (2)$$

where ξ is the displacement of the free surface and v_n is the component of velocity normal to the surface.

The main difficulties in describing granular flows center around the constitutive relationships for stresses σ_{ij} . These relationships differ drastically for flowing and static configurations of granular matter. For static regimes, the shear stresses are determined by the applied forces, whereas in fast and dilute granular flows the shear stresses are proportional to shear strain rates. The transition from one regime to another is controlled by so-called yield criteria, among which the most popular is the Mohr-Coulomb criterion relating shear and normal stresses. The goal of this paper is to unify the description of these different regimes of granular dynamics within a single theory. The central premise of our theory is that in partially fluidized flows, some of the grains are sliding past each other, while others maintain prolonged static contacts with neighbors. Accordingly, we write the stress tensor as a sum of the hydrodynamic part proportional to the flow strain rate e_{ij} , and the strain-independent part, σ_{ij}^s , i.e., $\sigma_{ij} = e_{ij} + \sigma_{ij}^s$. We assume that diagonal elements of the tensor σ_{ii}^s coincide with the corresponding components of the “true” static stress tensor σ_{ii}^0 for the immobile grain configuration in the same geometry, and the shear stresses are reduced by the value of the order parameter ρ characterizing the phase state of granular matter [29]. Thus, we write the stress tensor in the form

$$\sigma_{ij} = \eta \left(\frac{\partial v_i}{\partial x_j} + \frac{\partial v_j}{\partial x_i} \right) + \sigma_{ij}^s. \quad (3)$$

Here η is the viscosity coefficient, $\sigma_{ij}^s = \rho \sigma_{ij}^0$ for $i \neq j$, and $\sigma_{ii}^s = \sigma_{ii}^0$. In a static state, $\rho = 1$, $\sigma_{ij} = \sigma_{ij}^0$, $v_i = 0$, whereas in a fully fluidized state $\rho = 0$, and the shear stresses are simply proportional to the strain rates as in ordinary fluids.

To complete the set of governing equations, we need to introduce constitutive relations for components of the static shear stress tensor σ_{ij}^s , as well as an equation for the order parameter ρ . The issue of constitutive relations in static

granular configurations is rather complex and not completely understood [4,30]. It appears that in many cases the constitutive relations are determined by the construction history [31]. Recent studies elucidated the fundamental role of the force chain networks in the formation of the shear stress tensor [32]. We will assume that for any given problem, the corresponding static constitutive relation has been specified.

Since in dense granular flows the energy is rapidly dissipated due to inelastic collisions, we apply pure dissipative dynamics for the order parameter ρ , which can be derived from the free-energy-type functional \mathcal{F} :

$$\frac{D\rho}{Dt} = - \frac{\delta \mathcal{F}}{\delta \rho}. \quad (4)$$

We adopt the standard Landau form for $\mathcal{F} \sim \int d\mathbf{r} [D|\nabla\rho|^2 + f(\rho, \phi)]$, which includes a “local potential energy” and the diffusive spatial coupling. The potential energy density $f(\rho, \phi)$ should have extrema at $\rho = 0$ and $\rho = 1$ corresponding to uniform solid and liquid phases. According to the Mohr-Coulomb yield criterion for noncohesive grains [4] or its generalization [32], the static equilibrium failure and transition to flow is controlled by the value of the nondimensional ratio $\phi = \max|\sigma_{nm}^0/\sigma_{nm}^0|$, where the maximum is sought over all possible orthogonal directions n and m in the bulk of the granular material. We simply use this ratio as a parameter in the potential energy for the OP ρ . Without loss of generality, we write the equation for ρ :

$$\tau \frac{D\rho}{Dt} = l^2 \nabla^2 \rho - \rho(1-\rho)F(\rho, \phi). \quad (5)$$

Here τ and l are the characteristic time and length, correspondingly. One can expect that the length l is of the order of the grain size and the time τ is the typical time between collisions. For dense gravity driven flows, this scale can be estimated as $\tau_g = \sqrt{l/g}$. Further, according to observations, there are two angles which characterize the fluidization transition in the bulk granular material, an internal friction angle $\tan^{-1}\phi_1$ such that if $\phi \leq \phi_1$ the static equilibrium is unstable, and the dynamic repose angle $\tan^{-1}\phi_0$ such that $\phi < \phi_0$, the dynamic phase $\rho = 0$ is unstable. Values of ϕ_0 and ϕ_1 depend on microscopic properties of the granular material, and in general they do not coincide. Typically there is a range in which both static and dynamics phases coexist (this is related to the so-called Bagnold hysteresis [16]). The simplest form of $F(\rho, \phi)$ which satisfies these constraints is $F(\rho, \phi) = -\rho + \delta$, where

$$\delta = (\phi^2 - \phi_0^2)/(\phi_1^2 - \phi_0^2). \quad (6)$$

Here we use a square of ϕ to avoid nonanalytical behavior at $\sigma_{xz}^0 = 0$. Rescaling $t \rightarrow t/\tau$ and $x_i \rightarrow x_i/l$ leads to

$$\frac{D\rho}{Dt} = \nabla^2 \rho + \rho(1-\rho)(\rho - \delta). \quad (7)$$

This equation completes the general formulation of the continuum theory for partially fluidized granular flows. In an

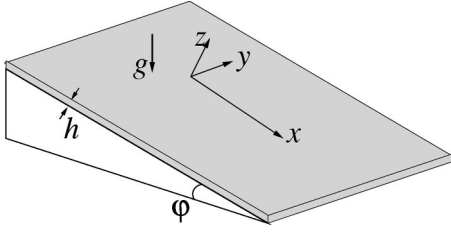


FIG. 1. Schematic representation of a chute geometry.

infinite system with fixed stress parameter $0 < \delta < 1$ ($\phi_0 < \phi < \phi_1$), both static ($\rho = 1$) and dynamic ($\rho = 0$) phases are linearly stable, and Eq. (7) possesses a moving front solution which connects these phases. The speed of the front in the direction of $\rho = 0$ is given by $V = (1 - 2\delta)/\sqrt{2}$. At $\delta = 1/2$ both phases coexist. For $\delta < 0$, only the solid phase survives, and at $\delta > 1$, only the liquid phase survives. The dynamics of partially fluidized granular flows becomes much more interesting in confined systems with fixed or free boundaries.

III. SHALLOW GRANULAR FLOW ON AN INCLINED PLANE

Let us now specialize our theory to the description of free-surface chute flows. We consider an initially flat layer of dry cohesionless grains of thickness h on a sticky surface tilted by angle φ to the horizon. We introduce a Cartesian coordinate frame aligned with the unperturbed (flat) surface of the tilted layer with the z axis normal to the surface and the x axis oriented downhill (see Fig. 1). Coordinate $z = 0$ corresponds to the position of the (unperturbed) free surface where the stress is absent, and $z = -h$ corresponds to the bottom of the layer. In case of the stationary shear flow in a flat layer, the force balance of Eq. (1) yields the following conditions:

$$\sigma_{zz,z} + \sigma_{xz,x} = -g \cos \varphi, \quad \sigma_{xz,z} + \sigma_{xx,x} = g \sin \varphi, \quad (8)$$

where the subscripts after commas mean partial derivatives. The solution to Eqs. (8) in the absence of lateral stresses $\sigma_{yy} = \sigma_{yx} = \sigma_{yz} = 0$ is given by

$$\sigma_{zz} = -g \cos \varphi z, \quad \sigma_{xz} = g \sin \varphi z, \quad \sigma_{xx,x} = 0. \quad (9)$$

Thus, in a stationary flow there is a simple relation between shear and normal stresses, $\sigma_{xz} = -\tan \varphi \sigma_{zz}$, independent of the flow profile. In a static equilibrium, the force balance also gives $\sigma_{xz}^0 = -\tan \varphi \sigma_{zz}^0$. Since by assumption $\sigma_{zz} = \sigma_{zz}^0$, we obtain $\sigma_{xz} = \sigma_{xz}^0$. In a flowing regime, the total stresses are composed of the static contribution in the viscous strain-related terms. According to our conjecture, the same relation holds between the static parts of the stress in the flowing regime. In this section, we will consider the non-stationary process of avalanche flow, but we will assume that this simple constitutive relation between shear and normal stresses is maintained in this regime as well, and deviations from the stationary stress distribution are small. For the flat layer of constant thickness, the value of parameter ϕ in Eq. (6) can be easily specified. In this case, the most unstable

yield direction is parallel to the inclined plane, so we can simply write $\phi_* = |\sigma_{xz}^0 / \sigma_{zz}^0| = \tan \varphi$. In the following, we will consider spatially and temporally inhomogeneous granular flows. In such flows the layer thickness varies, and the parameter ϕ becomes a variable determined by the local slope of the free surface. We will limit ourselves with the case of small deviations of the local slope from the unperturbed value ϕ_* , i.e., $|\partial_x h| \ll \tan \varphi$.

Let us now discuss the boundary conditions for the order parameter and velocity. At the bottom $z = -h$ we set $\rho = 1$, since the granular medium should be in a solid phase near the no-slip surface. The boundary condition at the free surface is less clear. Bearing in mind that the order parameter is related to the local entropy of grain configurations, and assuming zero entropy flux at the free surface, we choose the no-flux boundary condition for the order parameter $\rho_z = 0$.

All components of velocity should be zero at the bottom $z = -h$. The kinematic boundary condition (2) on the free surface for an incompressible medium can be expressed in the form of the mass conservation law

$$\partial_t h = -(\partial_x J_x + \partial_y J_y), \quad (10)$$

where $J_{x,y} = \int_{-h}^0 v_{x,y} dz$ are in-plane components of the flux of the granular material. In a typical situation of the chute flows, the downhill velocity v_x is much larger than the orthogonal y component v_y , so the mass conservation constraint can be simply expressed as

$$\partial_t h = -\partial_x J. \quad (11)$$

The velocity v_x is determined from the order parameter via Eq. (3) with the no-slip boundary condition $v_x = 0$ at $z = -h$.

The mass conservation law Eq. (11) can be rewritten in terms of the variable δ , which is related to the gradient of the local thickness $\partial_x h = \phi - \phi_*$. If we assume that the difference between the critical values $\phi_{0,1}$ is small, $(\phi_1 - \phi_0)/\phi_1 \ll 1$, which is the case for most granular flows, and the plane tilt is close to critical, $\phi \approx \phi_{0,1}$, from Eq. (6) we obtain (see also Fig. 1)

$$\phi = \partial_x h \approx -\frac{1}{\beta}(\delta - \delta_0), \quad (12)$$

where $\beta = 1/(\phi_1 - \phi_0) > 0$ and $\delta_0 = \text{const}$ corresponds to the flow with constant thickness h . Substituting Eq. (12) into Eq. (11) one derives

$$\partial_t \delta = \beta \partial_x^2 J. \quad (13)$$

This equation should be used instead of the conservation law (11) for infinitely deep layers (sandpiles or heaps), where the thickness h is not defined.

Because of the no-slip boundary condition at the bottom of the chute, for shallow layers the flow velocity is small, so the convective flux of the order parameter can be neglected (see Sec. III B for details), and the material derivative $D\rho/Dt$ in Eq. (7) can be replaced by $\partial_t \rho$,

$$\partial_t \rho = \nabla^2 \rho + \rho(1-\rho)(\rho-\delta). \quad (14)$$

However, for fast flows this term may become important, see discussion below in Sec. IV B.

A. Stationary solutions and their stability

Let us first consider the granular flow in a uniform layer of constant thickness h . In this case $\delta = \delta_0$ is a constant, compare Eq. (12). There always exists a stationary solution to Eq. (14), $\rho = 1$, corresponding to a flat layer of constant thickness h at the static equilibrium, which obviously satisfies boundary conditions $\rho(-h) = 1, \partial_z \rho(0) = 0$. For $\delta > 1$ it is stable at small h , but loses stability at a certain critical thickness $h_c > 1$. The most “dangerous” mode of instability satisfying the above boundary conditions is of the form $\rho = 1 - A e^{\lambda t} \cos(\pi z/2h)$, $A \ll 1$. The eigenvalue of this mode is

$$\lambda(h) = \delta - 1 - \pi^2/4h^2. \quad (15)$$

Hence the neutral curve $\lambda = 0$ for the linear stability of the solution $\rho = 1$ is given by

$$h_c = \frac{\pi}{2\sqrt{\delta-1}}. \quad (16)$$

For $h > h_c(\delta)$ grains spontaneously start to roll, and a granular flow ensues.

In addition to the trivial state $\rho = 1$, for large enough h there exist nontrivial stationary solutions satisfying the above BC. These solutions correspond to the bold lines in the phase plane plots, Fig. 2. These solutions describe stationary granular flows supported by a constant supply of granular material upstream. For $1/2 < \delta < 1$ there exists a separatrix of the saddle $\rho = 1, \rho_z = 0$, which corresponds to the localized near-surface flow in an infinitely deep layer.

The velocity profile corresponding to a stationary profile of $\rho(z)$ can be easily found from Eq. (3) taking into account that $\sigma_{xz} = \sigma_{xz}^0$,

$$\frac{\partial v_x}{\partial z} = (1-\rho)\sigma_{xz}^0 = -\mu(1-\rho)z, \quad (17)$$

where $\mu = g \sin \phi / \eta$. The flux of grains in the stationary flow J is given by

$$\begin{aligned} J &= \int_{-h}^0 v_x(z) dz = -\mu \int_{-h}^0 \int_{-h}^z [1-\rho(z')] z' dz' dz \\ &= \mu \int_{-h}^0 z^2 (1-\rho) dz. \end{aligned} \quad (18)$$

The flux of supplied granular material J controls the thickness of the layer and the velocity profile. Figure 3 shows the thickness of the layer as a function of flux J at several values of δ . For a fixed J , there are two values of h which correspond to two different regimes of granular flow on an inclined plane. The lower branch corresponds to the flow which involves the whole layer, while the upper branch corresponds to a flow which is localized near the surface.

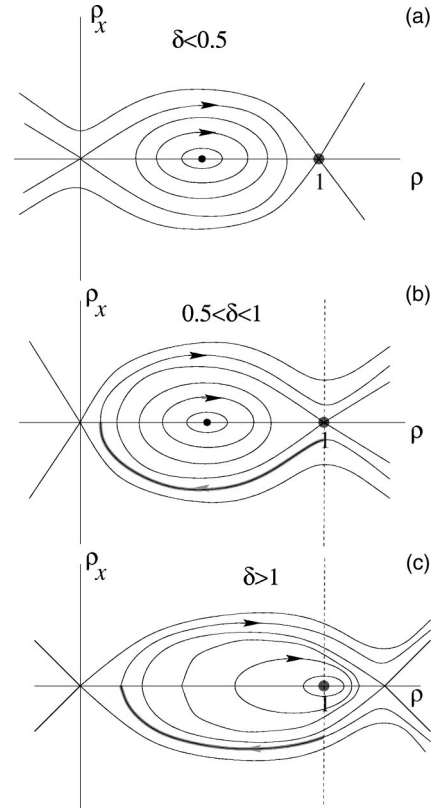


FIG. 2. Phase plane of stationary Eq. (14) for three typical values of δ : (a) $\delta < 0.5$, (b) $0.5 < \delta < 1$, and (c) $\delta > 1$.

Profiles $\rho(z)$ corresponding to the different branches at the same value of the flux are shown in Fig. 3(b). The selection and the stability of these solutions depend strongly on the particular problem at hand. Since for fixed h Eq. (14) has a free-energy functional [see Eq. (4)], $\mathcal{F} = \frac{1}{2}[\rho_z^2 + \rho^4/2 + \delta\rho^2 - 2/3(\delta+1)\rho^3]$, stable solutions should correspond to the minimum of \mathcal{F} . It is easy to check that the lower branch corresponds to the minimum of the free energy \mathcal{F} , and therefore it is stable, whereas the upper branch is unstable (corresponds to the maximum of \mathcal{F}). If the flux J is fixed by the boundary condition at $x=0$, the corresponding unstable mode, which at large h is close to the translation mode $\partial_z \rho$, is prohibited because it would violate the mass conservation constraint. However, even in this case the solutions corresponding to the upper branch can be unstable with respect to spatially nonuniform perturbations. Actually, it can be easily shown that this type of instability occurs for parts of the upper branch solutions corresponding to $dJ/d\delta < 0$. Indeed, assuming small deviations of the local slope, we can linearize Eq. (13),

$$\partial_t \delta_1 = \beta \frac{\partial J}{\partial \delta} \partial_x^2 \delta_1, \quad (19)$$

where $\delta_1 = \delta - \delta_0$. For $\partial J/\partial \delta < 0$ it is a diffusion equation with a negative diffusion coefficient, which is subject to a long-wavelength instability. On the other hand, if the slope of the free surface is fixed everywhere, this instability is also suppressed.

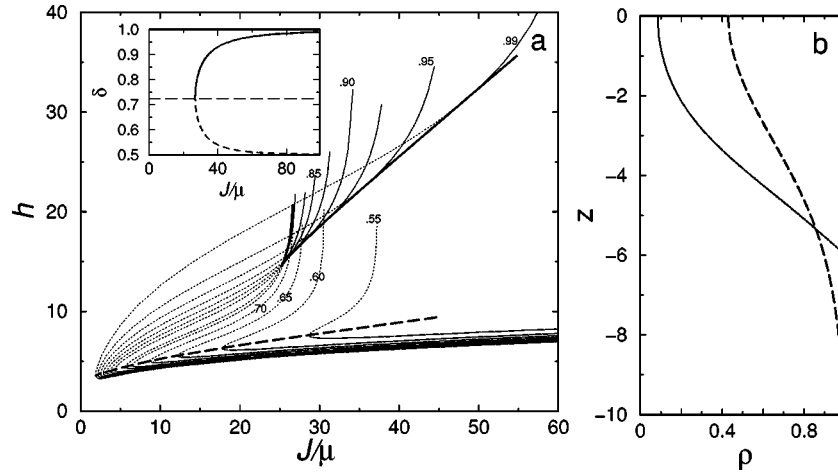


FIG. 3. Bifurcation diagram of the stationary flow regimes with a fixed granular flux. (a) Thickness of the layer h as a function of J/μ at several δ (the value of δ is shown near each line). The parts of the curves corresponding to unstable solutions are shown by dashed lines. The thick line, given by the envelope condition $\partial J(h, \delta)/\partial \delta = 0$, separates stable and unstable parts of the upper branches. Thick dashed line shows the stability exchange line $\partial J(h, \delta)/\partial h = 0$. Inset: Normalized slope δ vs flux J/μ for infinitely deep chute ($h \rightarrow \infty$), the OP ρ is given by Eq. (21). The branch below the dashed line [the condition $dJ(\delta)/d\delta = 0$] is unstable. (b) Vertical profiles $\rho(z)$ corresponding to the lower (solid) and upper (dashed) branches at the same value of flux ($J/\mu = 23.0$) for $\delta = 0.65$.

The two branches merge at the minimum value $h_s(\delta)$, where $dJ/dh = 0$. At $h < h_s$, there is no stationary granular flow solution and only nonstationary regimes are possible (see below). The value of h_s can be found as a minimum of the following integral as a function of ρ_0 , the value of ρ at the surface $z = 0$,

$$h_s = \min_{\rho_0} \int_{\rho_0}^1 \frac{d\rho}{\sqrt{\frac{\rho^4}{2} - \frac{2(\delta+1)\rho^3}{3} + \delta\rho^2 - c(\rho_0)}}, \quad (20)$$

where $c(\rho_0) = \rho_0^4/2 - 2(\delta+1)\rho_0^3/3 + \delta\rho_0^2$. This integral can be calculated analytically for $\delta \rightarrow \infty$ and $\delta \rightarrow 1/2$. It is easy to show that for large δ , the critical solution of Eq. (14) has a form $\rho = 1 + A \cos(kz)$ with $A \ll 1$ and $k = (\delta - 1)^{1/2}$, and therefore, $h_s(\delta) \rightarrow h_c(\delta)$. For $\delta \rightarrow 1/2$, the critical phase trajectory comes close to two saddle points $\rho = 0$ and $\rho = 1$, and an asymptotic evaluation of Eq. (20) gives $h_s = -\sqrt{2} \ln(\delta - 1/2) + \text{const}$. This expression agrees qualitatively with the empirical formula $\phi - \phi_0 \sim \exp[-h_s/h_0]$ proposed in Refs. [20,22].

The neutral stability curve $h_c(\delta)$ and the critical line $h_s(\delta)$ limiting the region of existence of nontrivial stationary granular flow solutions are shown in Fig. 4. They divide the parameter plane (δ, h) in three regions. At $h < h_s(\delta)$, the trivial static equilibrium $\rho = 1$ is the only stationary solution of Eq. (14) for the chosen BC. For $h_s(\delta) < h < h_c(\delta)$, there is a bistable regime, the static equilibrium state coexists with the stationary flow. For $h > h_c(\delta)$, the static regime is linearly unstable, and the only stable regime corresponds to the granular flow. This qualitative picture completely agrees with the recent experimental findings [20,22]. Moreover, for no-slip bottom BCs (corresponding to our $\rho = 1$), authors of Ref. [20] found a region of bistability in the parameter plane

(h, φ) which has a shape very similar to our stability diagram in Fig. 4 (see below Sec. III E).

As we mentioned above, the upper branches of the $h(J)$ curves in Fig. 3 correspond to the case of a near-surface flow. For large enough h this regime can become unstable with respect to a spontaneous change of the slope δ . As was outlined above, the change of stability occurs at a tangent point between a curve $h(J)$ and an envelope $h_e(J)$ to the family of curves $h(J)$ for various δ , where $\partial_\delta J = 0$. The instability

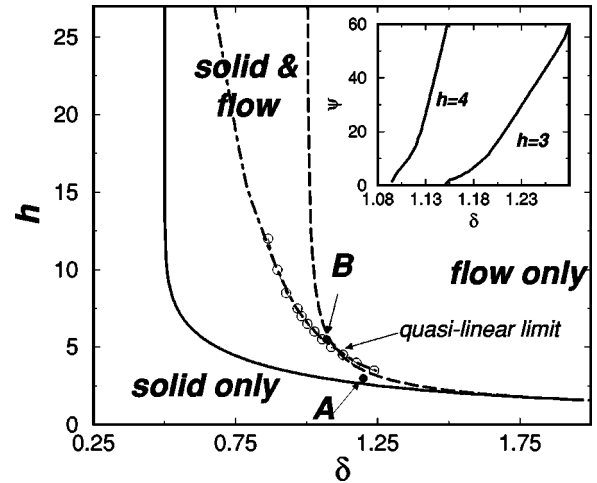


FIG. 4. Stability diagram. Dashed line shows neutral curve $h_c(\delta)$, Eq. (16), and solid line shows the existence limit of fluidized state $h_s(\delta)$, Eq. (20). Dot-dashed curve depicts the transition line from triangular to uphill avalanches obtained from solution of Eqs. (14) and (11) for $\mu = 0.4$ and $\beta = 0.25$. The line with circles shows the results obtained in quasilinear limit, Eqs. (24) and (25) (Sec. III B) for $\beta = 0.25$ and the value of μ which corresponds to $\alpha = 0.05$. Inset: opening angle of a downhill avalanche ψ (in degrees) vs δ for $\beta = 0.25$ and $\alpha = 0.015$ and two different values of the layer thickness.

would exhibit itself as accumulation of granular material near the top of the inclined plane leading to the change of slope. This process will result in an unlimited growth of local depth h , and at $t \rightarrow \infty$ the new stationary solution corresponding to $h \rightarrow \infty$ will be achieved. This regime can be described by an analytical formula which corresponds to the separatrix in Fig. 2(b) (cf. Ref. [33]):

$$\rho = \frac{\sqrt{(\delta+1)(\delta-1/2)} \cosh(z\sqrt{1-\delta}) + 2\delta - 1}{\sqrt{(\delta+1)(\delta-1/2)} \cosh(z\sqrt{1-\delta}) + 2 - \delta}. \quad (21)$$

In this deep-layer solution, the parameter δ , which corresponds to the slope of the free surface, is not related to the slope of the inclined plane (the free surface can be more or less steep than the underlying plane, as in sandpiles). Rather, δ is determined by the value of J . The dependence of the slope δ vs flux J for solution (21) is shown in Fig. 3, inset. The condition $J = \text{const}$ gives rise to two stationary values of δ . The upper branch approaches $\delta = 1$ as $J \rightarrow \infty$ as $J \sim 1/\sqrt{1-\delta}$. For the lower branch, the width of the fluidized zone z_0 , defined by $\rho(z=z_0) = 1/2$ is growing as $z_0 \sim \ln(\delta - 1/2)$ for $\delta \rightarrow 1/2$. Correspondingly, in this case one has the relation between the flux J and δ ,

$$J \sim \int_{-\infty}^0 z^2 (1-\rho) dz \sim z_0^3 \sim |\ln(\delta - 1/2)|^3. \quad (22)$$

Both branches merge at some minimum $J = J_c$. In the vicinity of J_c the flux and the angle are related as $J \approx J_c + \text{const} \times (\delta - \delta_c)^2 + \dots$. According to the condition $\partial J / \partial \delta > 0$, only the upper one corresponds to a stable near-surface flow, and the lower one corresponds to an unstable regime. In the stable regime, the slope of the sandpile increases with the flow, and for very large J the slope of the free surface δ approaches 1. This behavior agrees qualitatively with the observations of Ref. [28].

However, if the change of δ is limited, the instability of the lower branch can be suppressed. We believe that in Ref. [27], placing the mouth of the hopper supplying the sand directly on the surface of the sandpile limits the variation of δ and can possibly stabilize the lower branch. Moreover, since the instability is of a convective type, the length of the system may not be sufficient for it to develop.

At $J < J_c$ the stationary flow does not exist. In this regime the granular material accumulates and discharges in the form of avalanches periodically in time (see below Sec. III B). This phenomenology is also consistent with recent experiments in Refs. [28,34], where the transition from intermediate avalanches to a steady flow is reported. Moreover, as one expects from mass conservation, if the flow is represented by a periodic sequence of well-separated avalanches each carrying an amount of grain, the time between consequent avalanches should be $T_0 \sim J^{-1}$, in agreement with experiment [28]. Our theory predicts that at the onset of steady flow the angle of the sandpile should show critical behavior $\delta - \delta_c \sim \sqrt{J - J_c}$. However, in experiment [28] the critical transition has not been detected, possibly because the slope changes within a narrow range.

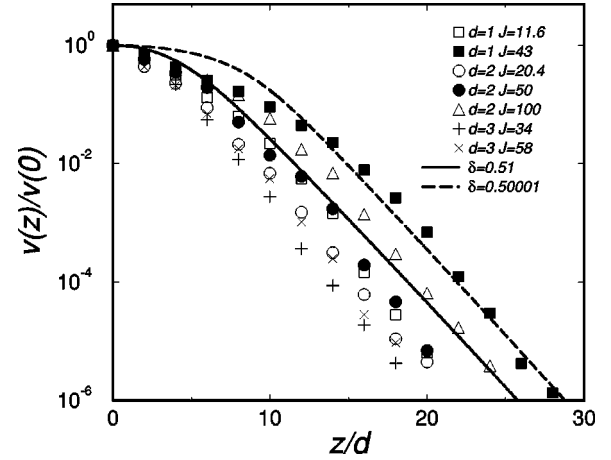


FIG. 5. Stationary velocity profiles $v(z)$ vs the distance from free surface z/d for different grain sizes d (mm) and supplied flux values J (g/sec) from Ref. [27]. The solid lines show theoretical results for two different values of δ .

Reference [28] also reports an increase of the width of the fluidized layer z_0 with increase of the applied flux J , which is consistent with Eq. (21). Also in agreement with the theory, the heap angle in Ref. [28] increased with J , which corresponds to the upper (stable) branch of the dependence $\delta(J)$ shown in Fig. 3, inset.

A similar transition is known for partially filled rotating drums when the rotation speed is varied. For low rotation speeds the flow in the drum occurs in the form of a periodic sequence of avalanches, whereas for larger rotation speeds a steady surface flow ensues [35]. We discuss this case below in Sec. IV C.

We compared the velocity profiles measured in Refs. [27,28] with our theory. The velocity can be determined from Eq. (17) using the expression for the order parameter (21). A typical velocity profile $v(z)$ vs z is shown in Fig. 5. For convenience we scaled $v(z)$ by the value at the open surface $v(0)$. In agreement with the experimental data the stationary profile has an exponential tail, i.e., $v(z) \sim \exp(-z/d_s)$, where $d_s = 1/\sqrt{1-\delta}$. For the lower branch of $\delta(J)$, which apparently describes the flow in the experiment by Komatsu *et al.* [27], the parameter δ at high flow rate approaches 1/2 (see inset of Fig. 3), i.e., the decay length $d_s = l\sqrt{2} \approx l/0.707$. Here l is the characteristic length in Eq. (5). The experimental value is $d_s \approx d/0.72$, which fixes the characteristic length equal to the grain size, i.e., $l = d$. Moreover, experimental data of Ref. [27] strongly indicate the independence of the decay length d_s on the value of flux in the wide range of flux values and grain diameter. This behavior again corresponds to the lower branch of $\delta(J)$ dependence. The value of the characteristic length l agrees with other independent experimental observations (see, for example, Refs. [20,22]).

Lemieux and Durian [28] also found exponential decay of velocity under surface: $v \sim \exp[-z/(0.15 \text{ cm})]$ for the grain diameter $d = 0.33 \pm 0.03$ mm. In their experiment, unlike Ref. [27], the particles were allowed to fall on the top of the sandpile, thereby relaxing the constraint on the slope of the sandpile. In this case, an upper branch of the function $\delta(J)$

should be selected, and for that branch the slope $\delta > 0.72$, so the characteristic decay length indeed should be larger than particle size d . In fact, it should be directly proportional to the flux J . It would be interesting to test this prediction in future experiments.

Pouliquen [22] proposed a scaling for the mean velocity $\bar{v} = J/h$ vs thickness of the layer h in the stationary flow regime, $\bar{v} \propto h^{3/2}/h_s$, which works for various angles φ as well as for different grain sizes, which is consistent with the so-called Bagnold scaling (see also results of large-scale molecular dynamics simulations in Ref. [5]). Equation (18) yields $v \propto (h - h_s)^{1/2}$ for small $h - h_s$ and $v \propto h^2$ for large h . It is plausible that the experimentally found scaling exponent 3/2 is the result of the crossover between the two different regimes. However, renormalization \bar{v}/\sqrt{gh} , h/h_s as in Ref. [22] does not collapse our results onto a single curve, perhaps due to the assumption of a simple Newtonian relation between the strain v_z and the hydrodynamic part of the shear stress σ_{xz} with a fixed viscosity η [see Eq. (3)]. In fact, the viscosity itself may depend on ρ and z in some fashion.

B. Nonstationary dynamics in a single mode approximation

In the vicinity of the neutral curve (16) Eqs. (1) and (14) can be significantly simplified. We may look for a solution in the form (compare Sec. III A)

$$\rho = 1 - A(x, y, t) \cos\left(\frac{\pi}{2h} z\right) + w, \quad (23)$$

where $A \ll 1$ is now a slowly varying function of t , x , and y , and $w \ll A$ is a small correction to the solution. At the neutral curve defined by the condition $\lambda(\delta, h) = \delta - 1 - \pi^2/4h^2 = 0$ the expression (23) with $A = \text{const}$, $h = \text{const}$ is an exact solution to the linearized Eq. (14). In the vicinity of the neutral curve defined by the condition $|\lambda| \ll 1$, the ansatz (23) with the slowly-varying functions A, h gives an approximate solution to the full Eq. (14). The function A itself is determined as a result of the orthogonality (or solvability) condition with respect to the function $\cos[(\pi/2h)z]$.

Substituting ansatz (23) into Eq. (7), one obtains in the first order in w the expression $\hat{L}w = \hat{H}$, where $\hat{L} = \partial_z^2 + \delta - 1$ is the linearized operator, and inhomogeneity \hat{H} does not contain terms linear in w and depends only on A and its derivatives. Applying the solvability conditions $\int_{-h}^0 \hat{H} \cos(\pi z/2h) dz = 0$, one obtains in the first order,

$$A_t = \lambda A + \nabla_{\perp}^2 A + \frac{8(2-\delta)}{3\pi} A^2 - \frac{3}{4} A^3 - \bar{\alpha} h^2 A \partial_x A, \quad (24)$$

where $\nabla_{\perp}^2 = \partial_x^2 + \partial_y^2$ and $\bar{\alpha} = \mu(3\pi^2 - 16)/3\pi^3 = 0.146\mu$. Equation (24) must be coupled to the mass conservation equation which reads as (here we neglect the contribution from the flux along the y axis $J_y \sim \partial_y h \ll J$):

$$\frac{\partial h}{\partial t} = -\frac{\partial J}{\partial x} = -\alpha \frac{\partial h^3 A}{\partial x}, \quad (25)$$

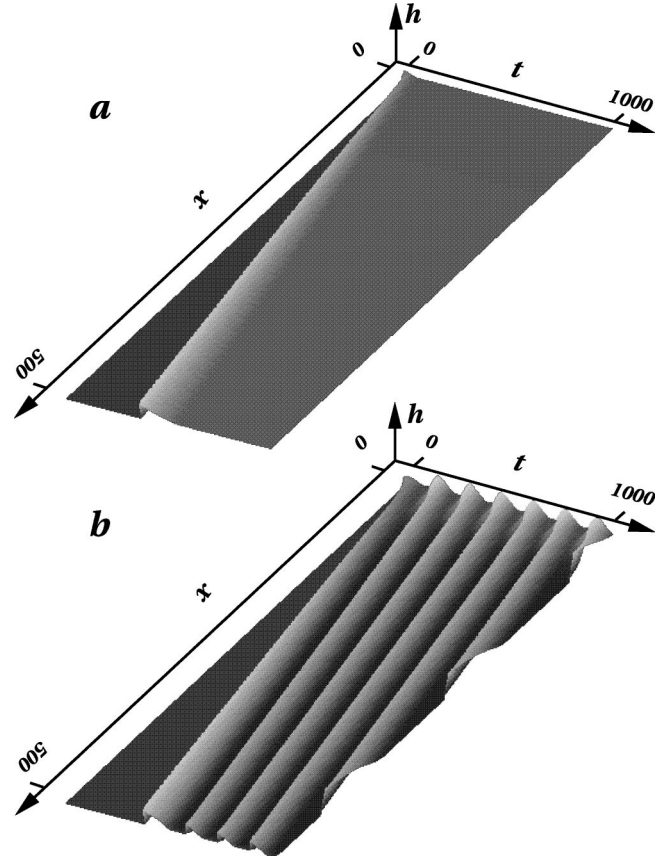


FIG. 6. Space-time surfaces showing the one-dimensional evolution of height h in a shallow chute for two values of the fixed supplied flux $J=0.6$ (a) and $J=0.4$ (b). Other parameters of the model are $\alpha=0.025, \beta=3.15, \delta=1$. The chute length $L=500$, number of grid points $N=1000$. Initial condition is $A=0, h=3$.

where J was calculated from Eq. (18) using ansatz (23) and $\alpha = 2\mu(\pi^2 - 8)/\pi^3 = 0.12\mu$. Taking into account that variations in h also change the local surface slope, we replace δ in Eq. (24) by $\delta_0 - \beta h_x$, see Eq. (12).

In deriving these equations we assumed that $(2-\delta)A^2$ and A^3 are of the same order, i.e., $\delta \approx 2$, however qualitatively a similar equation with a different nonlinearity can be obtained for any δ and h .

The last term in Eq. (24) originates from the convective term $v \nabla \rho$ in Eq. (7). For not very large thickness of the layer h and in the large viscosity limit $\mu \ll 1$ this term can be neglected with respect to other terms in Eq. (24). However, for thick layers the convective term cannot be neglected because the magnitude of this term grows as h^2 .

We studied Eqs. (24) and (25) numerically and analytically in one and two dimensions. First, we considered the flow with the fixed supplied flux in one dimension x . In this situation the flux $J = \text{const}$ is introduced via the boundary condition in Eq. (25) at $x=0$. For large values of the flux we indeed observed the transition to the steady flux regime [see Fig. 6(a)], although some transient avalanches occur, which are related to the adjustment of the chute thickness. For smaller values of the flux (below the corresponding cutoff value in Fig. 3), we find that the flow occurs in the form of a

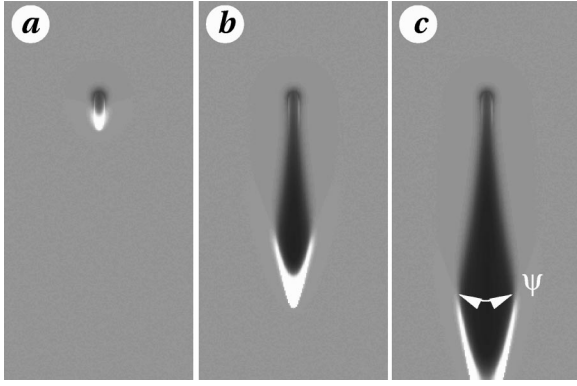


FIG. 7. Gray-coded images demonstrating the evolution of a triangular avalanche for $t=50$ (a), $t=200$ (b), and $t=250$ (c). White color corresponds to maximum height of the layer, and black to minimum height. Parameters of Eqs. (24) and (25) are $\alpha=0.15$, $\beta=0.25$, $\delta=1.2$, and $h_0=3$, point A in Fig. 4.

periodic sequence of avalanches, Fig. 6(b). Our numerical simulations indicate that the time between the avalanches T_0 diverges as $T_0 \sim J^{-1}$ at $J \rightarrow 0$, in agreement with experimental results of Ref. [28]. Moreover, we observed an abrupt hysteretic transition from avalanching to steady flow with the increase of supplied flux J , which also agrees with Ref. [28].

In order to study the evolution of avalanches in two dimensions (x, y) we performed simulations in a fairly large system, $L_x=400$ dimensionless units in the x direction (downhill) and $L_y=200$ units in the y direction, with the number of grid points being 1200×600 . As initial conditions we used a uniform static layer: $h=h_0, A=0$. We triggered avalanches by a localized perturbation introduced near the point $(x, y) = (L_x/4, L_y/2)$. Close to the solid line in Fig. 4 we indeed observed avalanches propagating only downhill, with the shape very similar to the experimental one [21] (see Fig. 7). The avalanche leaves a triangular track with the opening angle ψ in which the layer thickness h is decreased with respect to the original value h_0 . At the front of the avalanche the layer depth is greater than h_0 , as in experiment. The opening angle as a function of δ is shown in the inset of Fig. 4.

For larger values of δ or for thicker layers (close to the dashed line in Fig. 4) we observed avalanches of the second type (Fig. 8). In this case the avalanche zone expands both uphill and downhill. Unlike the previous case, the whole avalanche zone is in motion, as new rolling particles constantly arrive from the upper boundary of the avalanche zone. Sometimes we observed small secondary avalanches in the wake of the large primary avalanche, see Fig. 8(c).

C. Transition from triangular to uphill avalanches

Our model predicts the transition from triangular to uphill avalanches when the thickness of the layer or the inclination angle are increased, similar to that observed in experiment [20]. In order to investigate the transition in detail, we again return to the one-dimensional version of Eqs. (24) and (25). The results of the simulations are shown in Fig. 9.

As can be seen in Fig. 9(a), a finite perturbation introduced near $x=300$ triggers a downhill avalanche for smaller

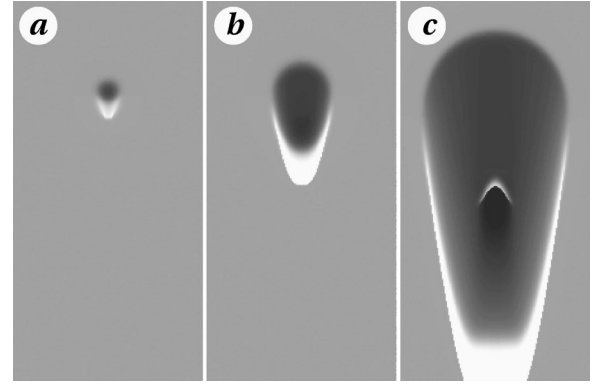


FIG. 8. Snapshots of an uphill avalanche for $t=40$ (a), $t=100$ (b), and $t=180$ (c). Parameters of Eqs. (24) and (25) are $\alpha=0.05$, $\beta=0.25$, $\delta=1.07$, and $h_0=5.5$, point B in Fig. 4. A small secondary avalanche is seen in the image (c).

δ . Due to mass conservation, the height of the avalanche increases as it propagates downhill.

For larger δ , the region of fluidized grains expands not only downhill, but also uphill [see Fig. 9(b)]. In contrast to the downhill avalanche, the uphill front appears to be a steady-state solution, $A=A(x+Vt), h=h(x+Vt)$. Our simulations show that the velocity of the front remains finite at the transition point, see Fig. 10. Since the uphill front always propagates with the finite velocity $V > V_0 > 0$, we call this phenomenon a “velocity gap.”

It can be shown from the analysis of Eq. (25) that the front solution indeed cannot exist for an arbitrarily small speed. In a comoving with velocity V frame, the front is a stationary solution, and Eq. (25) reads

$$V(h-h_0) = -\alpha h^3 A. \quad (26)$$

The nontrivial front solution must satisfy the boundary conditions $h \rightarrow h_0, A \rightarrow 0$ for $x \rightarrow -\infty$ and $h \rightarrow h_\infty, A = A_\infty \neq 0$ for $x \rightarrow \infty$, where

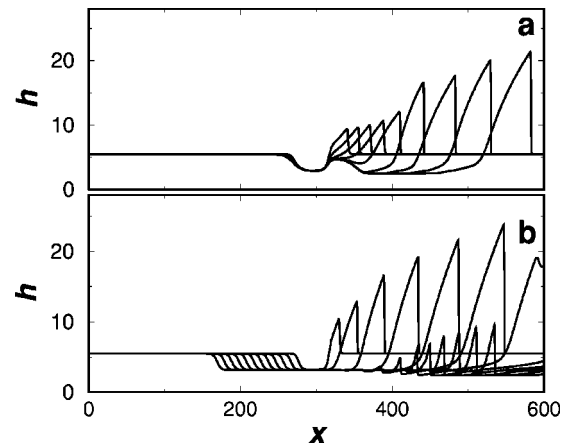


FIG. 9. One-dimensional evolution of a localized perturbation in a long shallow chute for two values of δ , (a) $\delta=1.02$; (b) $\delta=1.07$. Shown are the height profiles at ten consecutive moments of time for $h_0=5.5, \alpha=0.05, \beta=0.25$. Secondary avalanches are seen in panel (a).

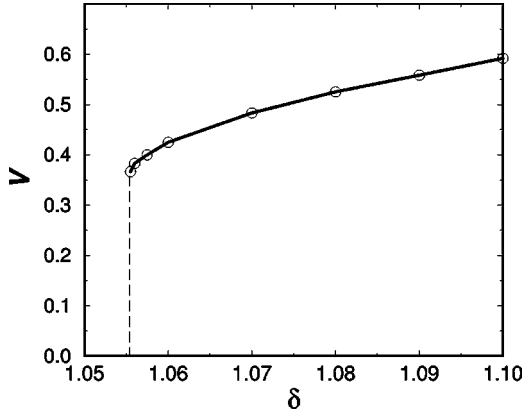


FIG. 10. The velocity of uphill front vs δ for $h_0=5.5, \alpha=0.05, \beta=0.25$. The cutoff value of velocity $V_0 \approx 0.35$.

$$A_\infty = \frac{16(2-\delta)}{9\pi} + \sqrt{\left(\frac{16(2-\delta)}{9\pi}\right)^2 + \frac{4}{3}\left(\delta - 1 - \frac{\pi^2}{4h_0^2}\right)}. \quad (27)$$

Since A_∞ cannot be arbitrarily small for finite h_∞ by the nature of the hysteretic transition from the solid to the fluidized state, V also cannot be arbitrarily small. Thus, our model predicts the velocity gap for the uphill front, which is in fact supported by the experimental data in Refs. [21,19]. This result appears to be in contradiction with the conjecture of Bouchaud and Cates [36] that the transition from triangular to uphill avalanches occurs at *zero* front velocity.

Tracking systematically the moving front existence limit in (δ, h) we obtained the line separating the triangular/uphill avalanches in the (δ, h) plane, see Fig. 4.

D. Uphill triangular avalanche transition and the velocity gap in the large viscosity limit

The above argument justifying the finite velocity gap is not valid in the limit of very large viscosity ($\alpha \rightarrow 0$). In this case, the thickness of the layer does not change ($h=h_0 = \text{const}$), and the order-parameter equation (14) becomes independent. The uphill front solution $\rho(x+Vt, z)$ satisfies the equation

$$V\rho_x = \nabla^2 \rho - \rho(1-\rho)(\delta-\rho). \quad (28)$$

In this case, the transition between uphill and downhill front propagation is continuous, and it corresponds to the $V=0$ solution of Eq. (28). This solution exists only for a specific value of δ corresponding to the layer thickness h . The dependence $\delta(h)$ is derived in Appendix A. At large h_0 it results in

$$h \sim \frac{\ln(\delta - 1/2)}{\delta - 1/2}, \quad (29)$$

i.e., at large h the region of uphill avalanches shrinks, in agreement with experiments [20].

For small $h=O(1)$, the transition line can be found from the stationary solution of single-mode approximation Eq. (24). In this case,

$$h = \frac{\pi}{2} \frac{1}{\sqrt{\delta - 1 + \frac{2}{3}\left(\frac{16}{9\pi}(2-\delta)\right)^2}} \quad (30)$$

(see Appendix A).

For small but finite α (large viscosity η), the velocity gap is small [$O(\alpha^{1/2})$], and can also be found analytically from Eqs. (24) and (25).

At small $\alpha \ll 1$, the uphill front speed satisfies the following equation (see Appendix B):

$$V - \tilde{\delta}d_1 + \frac{\alpha d_2}{V} = 0, \quad (31)$$

where $\tilde{\delta} = \delta - \delta^*$ and δ^* is determined from the $V=0$ condition at $\alpha=0$, and $d_{1,2}$ are specified in Appendix B. From Eq. (31) we find

$$V = \frac{d_1 \tilde{\delta}}{2} + \sqrt{(d_1 \tilde{\delta})^2/4 - \alpha d_2} \quad (32)$$

(the branch with “ $-$ ” sign in front of the square root is unstable). Thus, the cutoff value of the velocity $V_0 = d_1 \tilde{\delta}/2$ and corresponding value of δ at the threshold of uphill propagation is

$$\delta = \delta^* + 2\sqrt{\alpha d_2}/d_1. \quad (33)$$

The above expansion, however, is valid only for very small α obeying the condition $\alpha h^3 \ll 1$.

E. Comparison with experiment

In order to establish a link between our theory and the experiments we need to specify the parameters ϕ_0 and ϕ_1 , as well as characteristic length l and time τ , and the viscosity η . Parameter ϕ_1 can be easily determined from the value of the chute angle corresponding to the vertical asymptote of the stability curve on the experimental bifurcation diagram of Ref. [20]. The value of ϕ_0 cannot be directly read from the bifurcation diagram. However, the vertical asymptote to the line bounding the region of existence of avalanches in Ref. [20], gives the value of the angle $\tilde{\phi}_0$ at which the front between the granular solid and fluid does not move, i.e., $\delta = 1/2$. Thus we can express our parameter δ through $\tilde{\phi}_0, \phi_1$. For the experimental parameters of Ref. [20], $\tan^{-1} \tilde{\phi}_0 \approx 25^\circ$ and $\tan^{-1} \phi_1 \approx 32^\circ$. It gives $\beta \equiv 1/2(\phi_1 - \tilde{\phi}_0) \approx 3.15$. Based on the comparison with experimental results for velocity decay in stationary flow from Ref. [27], as a characteristic length l we can take the mean diameter of the grain d , which for the experiment of Ref. [20] was 0.24 mm. Solid and dashed lines in Fig. 11 indicate theoretical stability boundaries, which correspond very nicely to the experimental findings.

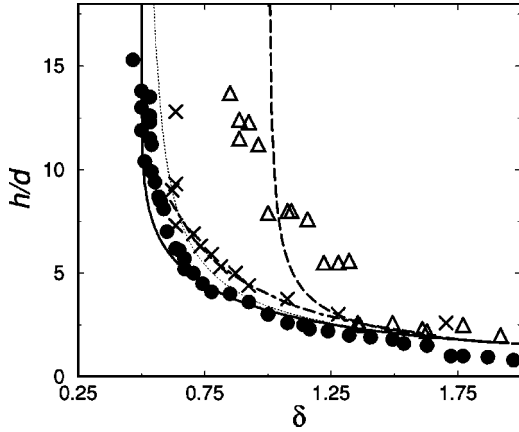


FIG. 11. Comparison of theoretical and experimental phase diagrams. Lines obtained from theory, symbols depict experimental data from Ref. [20]. Solid line and circles limit the range of existence of avalanches, long-dashed line and triangles correspond to the linear stability boundary of the static chute, and the dot-dashed line and crosses denote the boundary between triangular and uphill avalanches for $\beta=3.15, \alpha=0.025$ (or, correspondingly, $\mu=0.2$). Dotted line shows infinite viscosity limit $\eta \rightarrow \infty$.

The position of the line separating the triangular and uphill avalanches depends on the value of parameter α in Eq. (25). In fact, $\alpha \sim \tau/\eta$ is the only fitting parameter in the theory. In principle, it could be determined independently if we knew the characteristic time and the viscosity, but this data is not available to us. We find from the numerical solution of Eqs. (24) and (25) that the best fit to experimental data occurs for $\alpha \approx 0.025$ (correspondingly $\mu \approx 0.2$). For this choice we find a good agreement between theory and experiment (dotted line in Fig. 11).

IV. FLOWS IN DEEP GRANULAR LAYERS

A. Avalanches in deep chutes

In deep granular layers our assumption that the convective flux of the order parameter is small, is no longer valid, and we have to return to Eq. (7). As before, we choose the Cartesian coordinate system aligned with the unperturbed free surface with the origin at the surface, the z axis normal to the surface, and the x axis running downwards along the surface. For smooth horizontal variations of the flow, its local vertical profile can be approximated by the following dependence at $-\infty < z < 0$:

$$\rho = 1 - \{\tanh[(z+z_0)/\sqrt{8}] - \tanh[(z-z_0)/\sqrt{8}]\}/2 \quad (34)$$

with a slowly varying depth of the fluidized layer z_0 . This expression is very close to the exact front solution

$$\rho = \frac{1}{2}(1 \pm \tanh[z/\sqrt{8}]) \quad (35)$$

if $z_0 \gg 1$ and $\delta \rightarrow 1/2$ and differs from it only in the vicinity of the free surface $z=0$, where it is augmented in order to sat-

isfy the no-flux boundary condition $\partial_z \rho = 0$. Moreover, for $z_0 \rightarrow 0$ one has $\rho \rightarrow 1$, thus one recovers the behavior of the linearized Eq. (7).

Let us introduce the new variable

$$\bar{z} = \int_{-\infty}^0 (1-\rho) dz. \quad (36)$$

It is easy to check that for ansatz (34), $\bar{z} = z_0$. We will show below that the simplified description of the dynamics of Eq. (7) in the framework of \bar{z} is rigorous in two important limits: $\bar{z} \gg 1$ and $\bar{z} \ll 1$. For the intermediate values of \bar{z} the above approximation for the order-parameter equation (34) gives smooth interpolation between these two limits. Our numerical simulations indicate that qualitative features are not sensitive to the specific choice of interpolation since the solution tends to “avoid” the intermediate area (we obtained qualitatively similar results using piece-linear approximations).

After integration of Eq. (7) we obtain

$$\partial_t \bar{z} = \partial_x^2 \bar{z} + \int_{-\infty}^0 \rho(1-\rho)(\delta-\rho) dz + \int_{-\infty}^0 (v_x \partial_x \rho + v_z \partial_z \rho) dz. \quad (37)$$

The horizontal velocity profile $v_x(z)$ is found from Eq. (17),

$$v_x = -\mu \int_{-\infty}^z (1-\rho) z' dz' \quad (38)$$

and

$$v_z = - \int_{-\infty}^z dz' \partial_x v_x = \partial_x z_0 \mu \int_{-\infty}^z dz' \int_{-\infty}^{z'} d\zeta \zeta \partial_\zeta (1-\rho). \quad (39)$$

Now, substituting Eqs. (34), (38), and (39) into Eq. (37), after some algebra we get

$$\partial_t z_0 = \partial_x^2 z_0 + F(z_0) - \mu G(z_0) \partial_x z_0. \quad (40)$$

Function $F(z_0)$ can be found in the closed form

$$F = \frac{6}{\sqrt{2}(s-1)} + \frac{2\delta-1}{\sqrt{2}} - \frac{2z_0}{s-1} \left(\frac{3}{s-1} + \delta + 1 \right) \quad (41)$$

with $s = \exp(\sqrt{2}z_0)$. Function $F(z_0)$ has the following asymptotic behaviors:

$$F(z_0) = \begin{cases} (\delta-1)z_0 & \text{for } z_0 \ll 1, \\ \sqrt{2} \left(\delta - \frac{1}{2} \right) & \text{for } z_0 \gg 1. \end{cases} \quad (42)$$

Thus, at small z_0 Eq. (37) complies with the behavior of Eq. (7), linearized near $\rho=1$ and for large z_0 Eq. (37) gives the asymptotically correct result for the velocity of the front between the fluidized and solid state at $\delta \rightarrow 1/2$.

Function $G(z_0)$ can only be found in an integral form. However, asymptotic values of $G(z_0)$ can be found for large and small z_0 ,

$$G(z_0) = \begin{cases} \frac{12 - \pi^2}{3\sqrt{2}} z_0 \approx 0.5021 z_0 & \text{for } z_0 \ll 1, \\ \frac{\pi^2}{3} \approx 3.29 & \text{for } z_0 \gg 1. \end{cases} \quad (43)$$

The expression for G , valid also for intermediate values of z_0 , can be approximated as

$$G(z_0) = \frac{\pi^2}{3} \tanh\left(\frac{12 - \pi^2}{\pi^2 \sqrt{2}} z_0\right). \quad (44)$$

This equation has to be solved together with the equation for δ . The latter can be derived from the mass conservation equation (11) with the expression for flux given by Eq. (18). Substituting $\rho(z)$ from Eq. (34), we obtain

$$\frac{\partial h}{\partial t} = -\frac{\mu}{3} \partial_x f(z_0), \quad (45)$$

where

$$f(z_0) = \begin{cases} 2\pi^2 z_0 & \text{for } z_0 \ll 1, \\ z_0^3 & \text{for } z_0 \gg 1. \end{cases} \quad (46)$$

We used the simplest interpolation for this function: $f(z_0) = z_0(z_0^2 + 2\pi^2)$. Differentiating Eq. (45) with respect to x , we arrive at the equation for δ [compare Eq. (13)],

$$\partial_t \delta = \frac{\mu\beta}{3} \partial_x^2 f(z_0). \quad (47)$$

Equations (40) and (47) give a simplified description of two-dimensional flows in deep inclined layers or sandpiles. We performed numerical simulations of avalanches within this model. We have found that small localized perturbations decay, and large enough perturbations trigger an avalanche. Figure 12 shows the development of the avalanche from a localized perturbation imposed at the point $x=480$. As it is seen from the figure, the avalanche propagates both uphill and downhill. This observation is consistent with our conclusion from previous sections that the domain of existence of triangular avalanches shrinks with the increase of layer thickness and is in agreement with experiment [19–21].

B. Connection with BCRE theory

It is interesting to point out the similarities and differences between our Eqs. (40) and (45) the set of phenomenological equations for avalanches in deep layers proposed earlier in Refs. [7–10].

The BCRE theory [9] operates with two variables, the thickness of immobile fraction H and the thickness of rolling (flowing) fraction R . These quantities obey the set of equations (see, e.g., Ref. [7])

$$\frac{\partial R}{\partial t} = -\gamma(\phi_r - \phi)R - \bar{v} \frac{\partial R}{\partial x} + D \frac{\partial^2 R}{\partial x^2}, \quad (48)$$

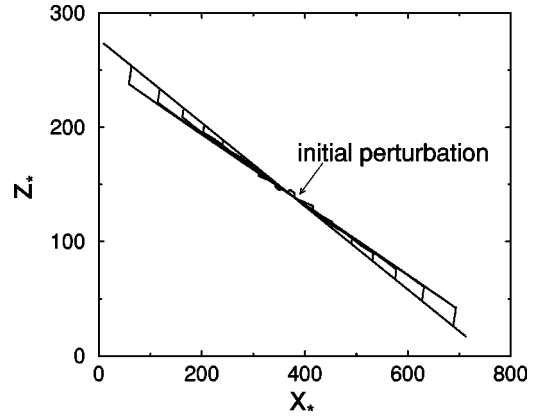


FIG. 12. Evolution of a free-surface profile during an avalanche within a simplified model (40),(47) for $\delta_0=0.75, \mu=0.2, \beta=3.15$, i.e., the parameters are the same as for Fig. 11. In the wake of the avalanche the slope of the free surface is reduced and approaches the equilibrium value $1/2$. Note the “true” horizontal and vertical variables (x_*, z_*), which are related to our original Cartesian variables (x, y) via a simple rotation by angle φ .

$$\frac{\partial H}{\partial t} = \gamma(\phi_r - \phi)R, \quad (49)$$

where ϕ_r is the critical slope, $\phi = -\partial H/\partial x$ is the local slope, term $\gamma(\phi_r - \phi)R$ describes the mass exchange between rolling (R) and static (H) layers, \bar{v} is the flow velocity (assumed to be constant) within the rolling layer, and D is the diffusion constant. The first BCRE equation (48) describes the dynamics of the rolling fraction, and Eq. (49) is analogous to our mass conservation law Eq. (45), although in our description h indicates the total thickness of the layer, i.e., $h = H + R$.

These equations were later modified in Refs. [10–12] for flows involving large values of R by replacing the instability term $\gamma(\phi - \phi_r)R$ by the saturation term $(\phi - \phi_r)v_{up}$ for $R > R_0, R_0 \gg 1$, yielding

$$\frac{\partial R}{\partial t} = (\phi - \phi_r)v_{up} + \bar{v} \frac{\partial R}{\partial x} + D \frac{\partial^2 R}{\partial x^2}, \quad (50)$$

where v_{up} is a constant of the order of \bar{v} . This modification provides layer thickness saturation at large R .

One may notice that Eq. (40) with Eqs. (41) and (44) coincide with the first BCRE equation (48) for $z_0 \ll 1$, and with Eq. (50) for large z_0 , however with one important caveat. From our derivation it directly follows that the value of the critical angle ϕ_r must be different for small and large R , whereas in Eqs. (48) and (50) that value is kept the same. This important distinction of our model gives rise to the hysteretic behavior of the fluidization transition, which is missing in the original BCRE model and its later modification [12].

In their recent work Aradian, Raphaël, and de Gennes [12] added phenomenologically the dependence of the velocity profile on the flowing layer thickness R . Note that in our approach this dependence appears naturally, however the

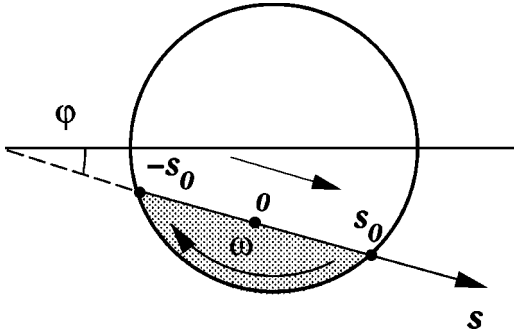


FIG. 13. Sketch of a flow in a rotating drum.

particular form of the coefficient G in the convective term in Eq. (40) differs from a simple linear form proposed in Ref. [12].

C. Flow in rotating drum

The dynamics of granular material placed in a rotating drum is another example of partially fluidized granular flow in a deep granular layer, see for review Ref. [34]. Depending on the rotation rate ω , see Fig. 13, the flow occurs in the form of a sequence of avalanches for small ω , or a steady flow for larger rotation speeds. At relatively small ω , the flow is confined to a narrow near-surface region, and the bulk exhibits rigid body rotation. These observations prompted a number of recently introduced continuum models [7,10,37–39] in which the flow was described by the dependence of its total flux on the local free-surface slope δ , $J \sim \delta - \delta_c$, where δ_c is the critical slope. This description yields rather realistic profiles of the free surface in the stationary flow regime, and also can explain the main features of segregation of binary granular mixtures in rotating drums [37–41]. However, it fails to describe the transition from periodic avalanching to the stationary regime. Evidently, this can only be done within a model which incorporates the hysteretic character of granular fluidization.

In this section we focus on the nonstationary granular flows in two-dimensional (2D) rotating drums, see Fig. 13. To simplify the description, we assume that the free surface profile is not very different from a straight line and the radius of the drum is much larger than the grain size. It allows us to use the formalism developed in Sec. IV A and reduce the description of the flow to the evolution of only two quantities: the position of the solid/liquid interface z_0 and parameter δ , which is proportional to $\tan \phi$.

The equation for z_0 is the same as in Sec. IV A:

$$\partial_t z_0 = \partial_s^2 z_0 + F(z_0, \delta) - \bar{v} \partial_s z_0, \quad (51)$$

where we introduced the coordinate s along the free surface and the convective term $\bar{v} \partial_s z_0$, see discussion above. This equation is subject to boundary conditions $z_0 = 0$ at the drum walls (say at $s = -s_0, s_0$). Since the flux $J \sim z_0$, this condition guarantees zero flux at the drum wall. The equation for δ is similar to Eq. (47), but has an extra term due to rotation (compare [7,38]):

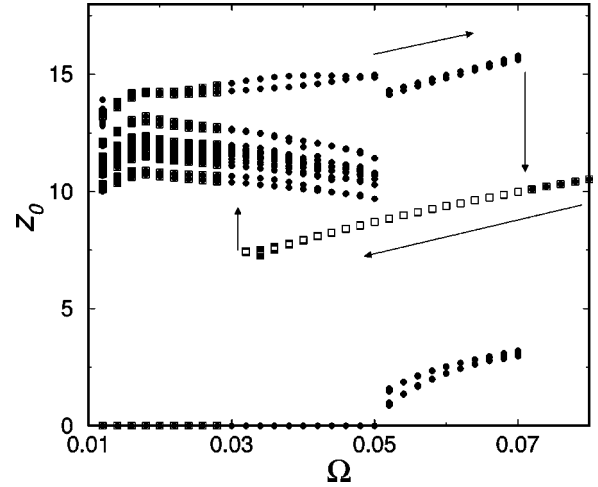


FIG. 14. Bifurcation diagram for the granular flow in a rotating drum obtained from the solution of Eqs. (51) and (52) for $\mu=0.2$, $\beta=3.15$, $-s_0 < s < s_0$, $s_0=100$. Symbols show z_0 at the center of the drum ($s=0$) at the moments when $dz_0/dt=0$; ● corresponds to increase of Ω , □ to decrease of Ω . The arrows illustrate the hysteretic transition between stationary and avalanche flows.

$$\partial_t \delta = \Omega + \partial_s^2 J, \quad (52)$$

where $J = (\mu\beta/3)f(z_0)$, compare Eq. (46), and Ω is proportional to rotation speed ω . The increase of the angle due to rotation is compensated by the flux of particles downhill described by the last term in Eq. (52).

We studied Eqs. (51) and (52) numerically. The deep-layer approximation is not valid near the edges of the free surface, i.e., for $s \approx \pm s_0$. It results in anomalous growth of the angle δ for $s \rightarrow \pm s_0$. In order to prevent this spurious behavior we add the regularization term $-[1 - \zeta(s)]\delta$ to Eq. (52). The function $\zeta(s)$ was chosen as follows: $\zeta = \tanh[\zeta_0(s_0 - |s|)]$, i.e., $\zeta \rightarrow 0$ near the edges and $\zeta = 1$ otherwise. This term enforces the decay of the variable δ near the edges of the drum. In our numerical simulations we used $\zeta_0 = 0.2$. We checked that the bulk behavior was not sensitive to the specific choice of the function $\zeta(s)$.

Some of the results are presented in Figs. 14–16. As seen in Fig. 14, for low rotation rates granular flow has a form of a sequence of avalanches separated by almost quiescent states ($z_0 \rightarrow 0$). Surprisingly, the time behavior, especially in large drums, at low rotation rates Ω is not strictly periodic, see Fig. 15, although one can distinguish a well-defined characteristic time between the avalanches, as in Refs. [35,42]. We think that this weak stochasticity in the form and the duration of individual avalanches in most cases is related to the noise amplification. Since the avalanches are separated by long quiescent periods when z_0 is extremely small (z_0 could be as small as 10^{-20} for $\Omega \ll 1$), the slope of free surface δ may “overshoot” the instability limit $\delta = 1$, and the system becomes susceptible to small fluctuations. These fluctuations trigger avalanches at random positions of the drum.

For higher rotation speed we observed the hysteretic transition to steady flow. In the steady flow regime ($\partial_t z_0 = \partial_t \delta = 0$) one finds from Eq. (52),

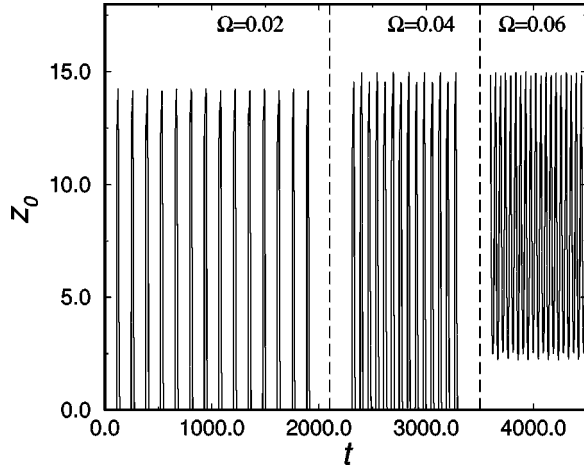


FIG. 15. The width of the fluidized layer z_0 vs time at the center of the drum in the regime of an avalanche flow for three different values of Ω , other parameters are the same as for Fig. 14.

$$J = \frac{\Omega}{2} (s_0^2 - s^2). \quad (53)$$

Using that $J \sim z_0^3$ [see Eq. (46)], one immediately finds the dependence of the depth of fluidized layer z_0 on the position along the drum surface s : $z_0 \sim \Omega^{1/3} (s_0^2 - s^2)^{1/3}$ (this expression is valid far from the edges, i.e., $|s| < s_0$). The dependence of z_0 vs s is shown in Fig. 16 for several values of angular rotation speed Ω . The dependence of z_0 vs s is practically symmetric with respect to the center of the drum, and z_0 increases with the rotation rate Ω in agreement with experiments (see, e.g., [43]). The form of z_0 vs s is consistent with recent experimental observations of flows in rotating drums from Ref. [44].

V. SHEAR GRANULAR FLOWS AND GRANULAR FRICTION

In this section we consider one-dimensional shear flow of granular matter placed between two parallel plates, one of

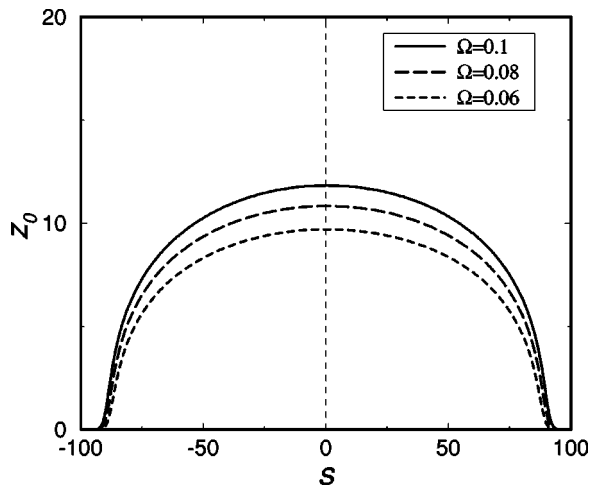


FIG. 16. Width of the fluidized layer z_0 vs s in the stationary flow regime for three values of Ω .

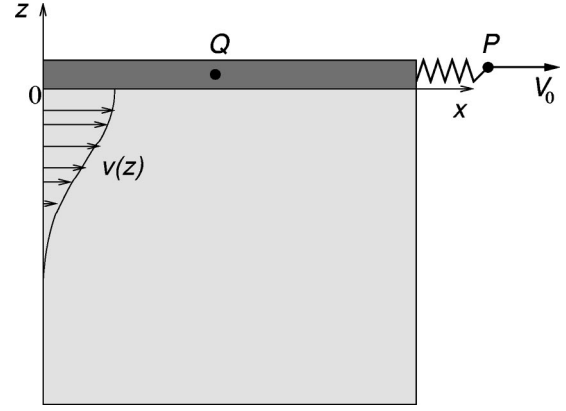


FIG. 17. Schematic representation of a 2D granular flow experiment. Granular material is driven by a heavy top plate which is pulled via a spring with constant velocity V_0 . The deflection of the spring is proportional to the difference between positions of “pulling point” P and plate displacement Q .

which is moving with the velocity V_0 (Couette flow). This flow (or rather Taylor-Couette flow between cylinders) has been studied in a number of recent experiments [23–26]. It was found that at small pulling speeds, granular flows exhibit nonstationary stick-slip motion [25]. At higher pulling speeds, the flow becomes stationary. The velocity profiles are typically exponential [23,26–28] in 2D experiments, but become Gaussian in 3D Taylor-Couette geometry [24]. We will show that these observations can be readily explained within our theoretical description.

A. 2D problem

In this section we neglect the effect of the (bottom) immobile boundary and restrict our analysis to the case of a planar shear flow in a semi-infinite layer of granular matter driven by a moving plate (see Fig. 17). We introduce a fixed Cartesian coordinate frame with horizontal axis x , vertical axis z , and the origin at the top of the granular layer. The general model is reduced to Eq. (14) combined with the constitutive relation

$$\sigma_{xz} = \eta \frac{dv}{dz} + \rho \sigma_{xz}^0, \quad (54)$$

where $v(z)$ is the horizontal velocity of the granular flow.

The relation for the control parameter δ reads as

$$\delta = \frac{(\sigma_{xz}^0 / \sigma_{zz}^0)^2 - \phi_0^2}{\phi_1^2 - \phi_0^2}, \quad (55)$$

where $\phi_{0,1}$ are tangents of the static and dynamic repose angles [compare with Eq. (6)]. Unlike the chute flow, the normal stress σ_{zz} is constant ($=1$), and the static component of the shear stress σ_{xz}^0 is independent of the depth z . Here we neglect the weight of the sand itself since the weight of the top plate provides a much larger normal stress. The independence of the static stress σ_{xz}^0 on z is in fact approximation. We assume that the “stress propagation time,” which is of

the order of collision time $\tau_0 \sim \sqrt{d/g}$ is much smaller than any time scale in our problem, which is true for moderate shearing rates.

The balance of forces requires $\sigma_{xz} = \sigma_{xz}^0$, which together with the constitutive relation (54) yields the expression for the shear velocity (one needs to set $\sigma_0 = \sigma_{xz}^0$ in order to satisfy the boundary condition at $z \rightarrow \infty$):

$$v(z) = \sigma_{xz}^0 \int_{-\infty}^z (1 - \rho) dz'. \quad (56)$$

These equations have to be augmented by the boundary conditions at $z \rightarrow \infty$ and $z = 0$. At $z \rightarrow \infty$ we require $\rho \rightarrow 1$, i.e., the granular material is static, and at $z = 0$, we require the no-flux condition $\rho_z(0) = 0$. We would like to note that in contrast to the analysis in Secs. III and IV, contact with the pulling plate is not equivalent to a free-surface condition, and therefore we cannot argue no-flux boundary conditions from the absence of an entropy flux. However, it seems to be the simplest *nontrivial* boundary condition possible. The other simple condition $\rho = \text{const} < 1$ would force permanent fluidization near the surface, which is clearly nonphysical, and the more general boundary condition $\rho + \text{const} \times \rho_z = 1$ yields qualitatively similar dynamics but introduces one more adjustable parameter.

In addition to that, we need a relation between the shear flow and the shear stress near the surface. We argue that as the plate moves, the shear stress at the boundary is proportional to the difference between the displacement of the pulling point $P(x_0 = V_0 t)$ and the displacement of the plate x_1 (point Q)

$$\sigma_{xz}^0 = \gamma(x_0 - x_1 - X_0), \quad (57)$$

where $\gamma = \text{const}$ is proportional to the spring stiffness and X_0 is a distance between P and Q corresponding to the unloaded spring (effective ‘‘Hooke’s law’’). Differentiating this equation with respect to time t yields the boundary condition

$$\dot{\sigma}_{xz}^0 = \gamma[V_0 - v(0)], \quad (58)$$

where we took into account that the plate velocity coincides with the velocity of grains immediately below the surface. Introducing scaled variables $S = \sigma_{xz}^0 / (\phi_1^2 - \phi_0^2)^{1/2} \sigma_{zz}^0$, $S_0 = \phi_0 / (\phi_1^2 - \phi_0^2)^{1/2}$, $\Gamma = \gamma \eta$, $W = V_0 \eta / (\phi_1^2 - \phi_0^2)^{1/2} \sigma_{zz}^0$, $V(z) = v(z) \eta / (\phi_1^2 - \phi_0^2)^{1/2} \sigma_{zz}^0$, we obtain the following set of equations:

$$\dot{\rho} = \nabla^2 \rho + \rho(1 - \rho)(\rho - S^2 + S_0^2), \quad (59)$$

$$V(z) = S \int_{-\infty}^z (1 - \rho) dz', \quad (60)$$

$$\dot{S} = \Gamma(W - V(0)). \quad (61)$$

It is interesting to trace the connection of our boundary condition (61) to the Maxwell stress relaxation condition for viscoelastic fluid [45],

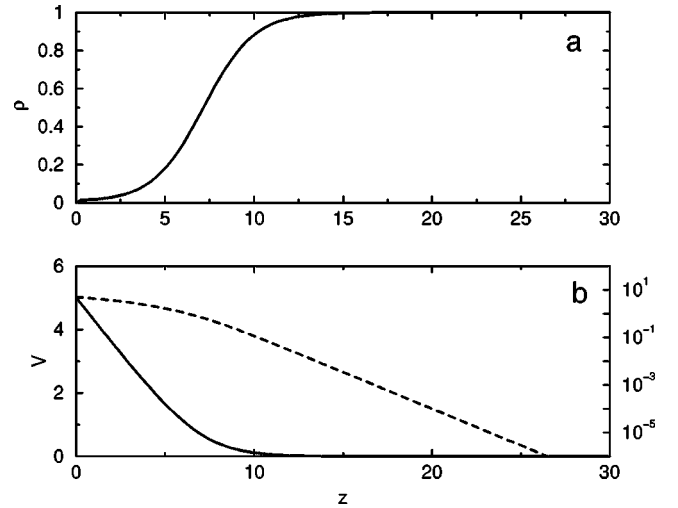


FIG. 18. Vertical profiles of the order parameter $\rho(z)$ (a) and the shear flow velocity $V(z)$ (b) for $S_0 = 0.1, \Gamma = 0.01, W = 5$. The solid line depicts the velocity profile in the linear scale and the dashed line depicts it in the semilogarithmic scale.

$$\frac{d\sigma_{xz}}{dt} + \frac{1}{\tau} \sigma_{xz} = \tilde{E} \frac{du_{xz}}{dt}, \quad (62)$$

where $\tilde{E} = \text{const}$ is the ‘‘effective shear modulus’’ and u_{xz} is the strain tensor, and τ is some characteristic relaxation time. It can be expected that τ is a function of the order parameter and diverges in solid state, $\rho \rightarrow 1$, so if we take

$$\tau = \Gamma / (1 - \rho) \quad (63)$$

and integrate Eq. (62) over z from $-\infty$ to 0, we get Eq. (61).

We integrated Eqs. (59)–(61) numerically using the finite difference method. The main control parameter of this model is the normalized velocity W . At large W we obtained a stationary near-surface shear flow with a profile shown in Fig. 18. In accordance with Eq. (60), the velocity V and the shear V_z are maximal near the surface, where ρ is minimal. For large z , the asymptotic velocity profile exhibits a well-defined exponential decay, Fig. 18(b). In fact, this stationary distribution of the order parameter ρ coincides with the exact solution Eq. (21), in which δ should be replaced by $S^2 - S_0^2$.

At small velocities $W \rightarrow 0$ the model exhibits relaxation oscillations, reminiscent of the normal dry friction between two solids. The stress σ_{xz} grows almost linearly with no flow until it reaches a certain threshold value after which the near-surface layer fluidizes, and the ensuing shear flow relieves the accumulated stress. After that the layer ‘‘freezes’’ again, and the process repeats (see Fig. 19).

Figure 20 depicts the bifurcation diagram illustrating the transition from the stationary shear flow at large W to the regime of relaxation oscillations at small W . As can be seen, the transition is subcritical with hysteresis (similar to the case of rotating drums), as the oscillations always occur with finite amplitude. A similar abrupt transition from oscillations to steady sliding was found in experiment Ref. [25].

Furthermore, we explored the dependence of the shear stress S on the pulling speed W . For the stationary flow re-

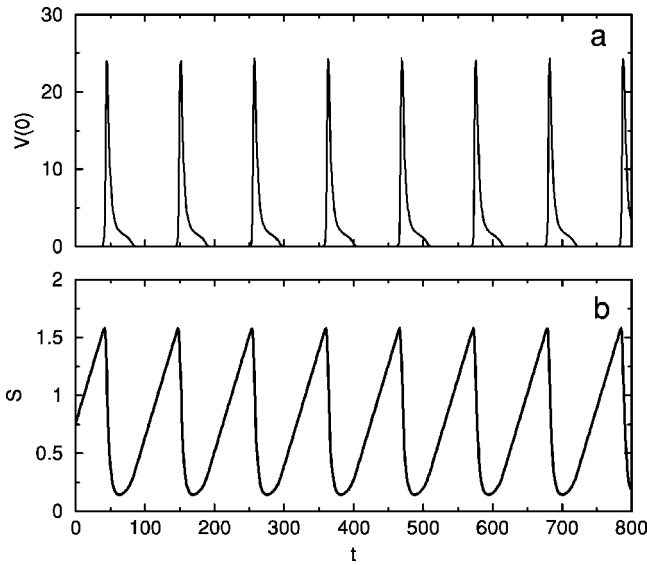


FIG. 19. Relaxation oscillations of the shear stress σ_{xz} (a) and the near-surface velocity $V(0)$ (b) for $S_0=0.1, \Gamma=0.01, W=2$.

gime it can be found analytically using the exact solution Eq. (21) for the order parameter ρ . A simple expression can be obtained at the large velocity limit ($W \gg 1$) corresponding to $\delta \rightarrow 1/2$. In this case one derives from Eqs. (21), (60), and (61),

$$W = S \int_{-\infty}^0 (1 - \rho) dz' \approx -\frac{S}{\sqrt{2}} \ln \left(\frac{\sqrt{S^2 - S_0^2} - 1/2}{6} \right). \quad (64)$$

As one sees from Eq. (64), with increase of the pulling velocity W the shear stress S monotonically decreases and approaches the value $S = \sqrt{1/2 + S_0^2}$, in agreement with the experimental results of Ref. [26], where it was also found that the shear stress slightly decreases with the increase of the shear rate and approaches some equilibrium value.

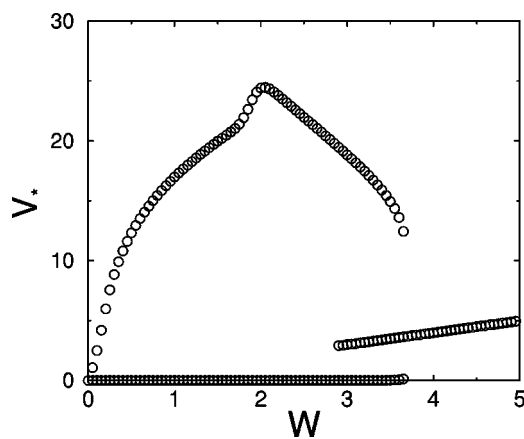


FIG. 20. Bifurcation diagram for the transition from stationary shear flow to relaxation oscillations. The dots in this plot depict the extrema of $V(t)$ as a function of the pulling speed W for $S_0 = 0.1, \Gamma = 0.01$. Periodic oscillations coexist with steady sliding for $2.6 < W < 3.6$.

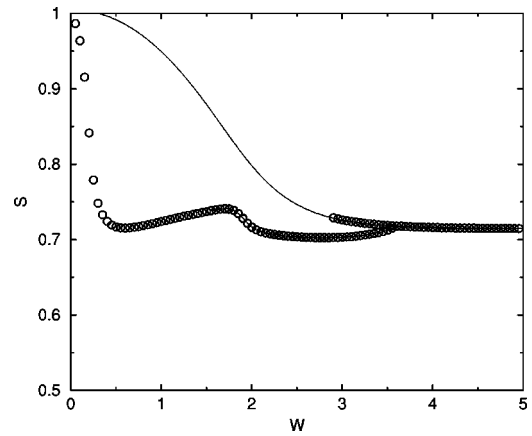


FIG. 21. Dependence of the normalized shear stress S on the pulling speed W for $S_0=0.1, \Gamma=0.01$ (circles). Nonuniqueness of this function is a result of the hysteretic transition from stick-slip motion to continuous sliding. The solid line corresponds to solution (64) for stationary shear flow regime.

The numerically obtained dependence of S vs W for arbitrary values of W is shown in Fig. 21. As seen from the figure, indeed there is only a weak dependence of S on W for $W > 0.5$.

In the recent paper [46], a model for the granular friction has been proposed, which is based on similar ideas of a phase transition in the granular medium underneath a moving surface. Within this model, oscillations in the form of stick-slip motion can be described, however the model does not describe the observed transition from stick-slip motion to the steady motion with the increasing of the pulling velocity. The significant difference between the model of [46] and our model is that the former does not address the spatial inhomogeneity of the fluidized layer, and thus the order-parameter dynamics is described by an ordinary differential equation. Second, the control parameter in the order-parameter equation [46] (see also [47]) is a function of the sliding velocity and not the applied stress, which in our opinion is not physical. Indeed, the transition to a fluidized state should be determined by a yield condition that is naturally defined via components of the stress tensor. Although in the dynamic friction problem the sliding velocity and the shear stress are related, we believe that the motion of the granular material is the consequence of the fluidization transition rather than the reason for it.

An alternative approach leading to the exponential decay of velocity in shear flows was developed in Ref. [26]. Using traditional hydrodynamic equations coupled to the equation for the granular temperature, the authors reproduced experimentally observed behavior. However, in order to explain the exponentially small velocity tail far away from the moving plate, a highly nonlinear viscosity with singular dependence on the density was introduced *ad hoc*. That model successfully describes the shear flow driven by a moving plate, however it fails to describe the transition between solid and fluidized states, which is the hallmark of the granular dynamics. Our model, on the contrary, is applicable to the description of both flowing and static regime.

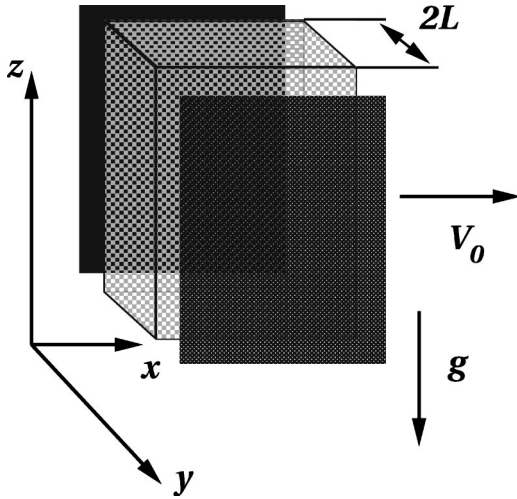


FIG. 22. Schematic representation of a 3D shear experiment. A slab of granular material is sandwiched between two vertical plates, one is moving with the speed V_0 at $y=0$ and one is immobile at $y=-2L$.

B. 3D problem

In this section we consider the 3D shear flow structure between two vertical plates one of which is moving with respect to the other (see Fig. 22). This geometry is inspired by the recent experiment by Mueth *et al.* [24] in which the structure of the granular shear flow was studied in a long vertical Taylor-Couette cell. In the experiment with rough particles they found a significant deviation in the shear flow profile from the simple exponential profile observed in earlier 2D experiments [23,25–28,48] and successfully reproduced by our theory (see the preceding section).

Reference [24] gives strong evidence for the Gaussian [$v \sim \exp(-\text{const} \times (r-r_0)^2)$] behavior of the velocity profile near the outer wall. As we show below, this feature can be attributed to the three-dimensional geometry of the experiment in contrast to that of Refs. [23,25–28]. It follows directly from the fact that the normal stress (pressure) in sufficiently long vertical cylinders filled with dry granular materials saturates and does not depend on the height of the cylinder (as in the celebrated Jansen picture of silo, see [3]).

Indeed, consider the distribution of stresses in an infinite layer of grains in contact with two vertical walls (gravity is directed along the z axis) at the points $y=0$ and $y=-2L$, see Fig. 22. From the projection of force on the z axis we obtain the condition

$$\sigma_{xz,x} + \sigma_{yz,y} + \sigma_{zz,z} = -g. \quad (65)$$

Since we assume that the diagonal component σ_{zz} does not depend on depth, i.e., the z coordinate, and there is no x dependence of stresses, we obtain that the weight is supported by the tangential stress $\sigma_{yz} = -g(y+L)$. Due to shearing we will also have tangential stress $\sigma_{xy} = \text{const}$, as in the two-dimensional case (with notational difference that y now indicates the direction normal to the walls).

Now, we need to relate the tangential stresses to the control parameter δ using the Mohr-Coulomb condition in three

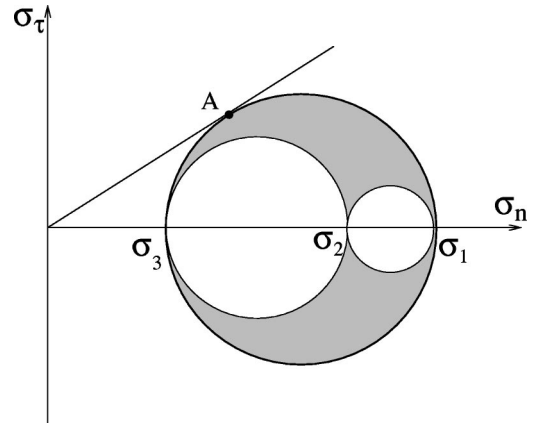


FIG. 23. Mohr's circle for the three-dimensional shear stress tensor [4].

dimensions. It is well known [4] that the tangential and normal stresses σ_τ and σ_n lie within the shaded area limited by the Mohr's circles built upon the major, intermediate, and minor principal stress values σ_{1-3} (see Fig. 23). As it is clear from Fig. 23, the maximum value of the ratio $\phi = \sigma_\tau / \sigma_n$ occurs at the tangential point A at which

$$\phi = \frac{\sigma_1 - \sigma_3}{2\sqrt{\sigma_1\sigma_3}}. \quad (66)$$

The major and minor principal stresses are determined as eigenvalues of the shear stress tensor σ_{ij} . The control parameter δ is related to ϕ via Eq. (6), so in this case

$$\delta = \left[\frac{(\sigma_1 - \sigma_3)2}{4\sigma_1\sigma_3} - \phi_0^2 \right] (\phi_1^2 - \phi_0^2). \quad (67)$$

For simplicity we assume that all diagonal components of the stress tensor are equal (like in fluid): $\sigma_{xx} = \sigma_{yy} = \sigma_{zz} = P = \text{const}$. This assumption makes the calculation much simpler, although qualitatively similar behavior is expected in the general case. Here P has the meaning of pressure at the bottom of the cell and from the dimensional consideration one concludes that $P \approx c_0 gL$, where $c_0 > 1$ is a constant that depends on surface wall roughness, etc. [3,31]. One obtains the eigenvalues

$$\begin{aligned} \sigma_1 &= P + \sqrt{g^2(y+L)^2 + \sigma_{xy}^2}, \\ \sigma_2 &= P, \\ \sigma_3 &= P - \sqrt{g^2(y+L)^2 + \sigma_{xy}^2}. \end{aligned} \quad (68)$$

Thus, one derives

$$\delta(y) = \frac{1}{\phi_1^2 - \phi_0^2} \left[\frac{g^2(y+L)^2 + \sigma_{xy}^2}{P^2 - g^2(y+L)^2 - \sigma_{xy}^2} - \phi_0^2 \right]. \quad (69)$$

Here, as before, σ_{xy} characterizes shear rate and is proportional to V_0 . Therefore, the control parameter δ in three dimensions has an explicit y dependence. In contrast, in 2D geometry we had simply $\delta = \text{const}$.

Let us now evaluate the decay rate of the order parameter. Linearizing Eq. (14) near $\rho=1$ we obtain

$$\rho_{yy} - \rho[1 - \delta(y)] = 0. \quad (70)$$

We focus on the solution near the wall $y=0$. If $|y/L| \ll 1$, we can apply the WKB approximation and seek the solution in the form $\rho \sim \exp[\Phi(y)]$. Then we derive $\Phi^2 = 1 - \delta(y)$. Therefore, for $0 < |y| \ll L$ and also for $\sigma_{xy}/P \ll 1$ we derive

$$\begin{aligned} \rho &= \exp \left[- \int_y^0 \sqrt{1 - \delta(y')} dy' \right] \\ &\approx \exp \left[\sqrt{1 - \delta(0)} y - \frac{\delta'(0)}{4\sqrt{1 - \delta(0)}} y^2 + O(y^3) \right] dy'. \end{aligned} \quad (71)$$

Thus, in three dimensions $\rho(y)$ possesses a Gaussian correction term, which is absent in two dimensions because $\delta' = 0$ in the 2D shear flow. Let us point out that, to the first order, the coefficient of y^2 does not depend on the shear rate in agreement with experiment [24].

VI. CONCLUSIONS

We developed a continuum theory of partially fluidized granular flows. This theory is based on a combination of the mass and momentum conservation laws with an equation for the order parameter describing the transition from the static to flowing regime. In this sense, our theory goes beyond the traditional hydrodynamical description of dense granular flows, see, e.g., [25,49–51]. The order parameter, which is a crucial variable in our theory, can be interpreted as a portion of the static contacts among particles in a small volume within the granular system. This quantity is difficult to measure in physical experiments, but can be extracted from molecular dynamics simulations. Phenomenological parameters in our model can be obtained from comparison with molecular dynamics simulations and experiments. In a certain limit our model can be reduced to two coupled equations for the depth of the fluidized layer and local angle, which resemble the BCRE model; however these differ from it when considered in detail. In particular, our model has intrinsic hysteretic behavior absent in the BCRE model.

Our order-parameter model captures many important aspects of the phenomenology of chute flows observed in recent experiments [20–22,27,28], including the structure of the stability diagram, the triangular shape of downhill avalanches at small inclination angles, and the balloon shape of uphill avalanches for larger angles. It provides an adequate description of granular flows in a 2D rotating drum and in a Couette geometry. In particular, we found the experimentally observed features such as periodic oscillations of the shear stress and the flow velocity at low rotation rates and the transition to a steady flow at higher rates. For sidewall-driven shear granular flows our model gives rise to the exponential velocity profile in two dimensions and the Gaussian correction to the profile in three dimensions.

A challenging project would be to derive the evolution equation for the order parameter from some sort of “microscopic” theory of granular flow, in analogy to the theory of superconductivity, where the order-parameter equation was first proposed phenomenologically by Ginzburg and Landau [52], and later derived from the microscopic theory of superconductivity by Gorkov and Eliashberg [53]. Since our model exhibits a critical slowdown for $\delta \rightarrow 1$, i.e., the decay length $d_s = d/\sqrt{1 - \delta}$ (or, pursuing the analogy with equilibrium critical phenomena, the coherence length) diverges at the critical point, an asymptotical derivation of the order-parameter equation can be anticipated in the vicinity of the point of spontaneous fluidization $\delta=1$.

ACKNOWLEDGMENTS

We thank Dan Howell, Saturo Nasuno, Doug Durian, Pierre-Gilles de Gennes, Jerry Gollub, Leo Kadanoff, Bob Behringer, and Adrian Daerr for useful discussions. This research is supported by the Office of the Basic Energy Sciences at the U.S. Department of Energy, Grant Nos. W-31-109-ENG-38, DE-FG03-95ER14516, and DE-FG03-96ER14592.

APPENDIX A: THE TRANSITION LINE BETWEEN TRIANGULAR AND UPHILL AVALANCHES—INFINITE VISCOSITY LIMIT

The transition line between triangular and uphill avalanches can be found analytically in the limit of infinite viscosity. In this case Eq. (11) yields a trivial solution $h=h_0 = \text{const}$ and Eq. (14) becomes independent. Within a single order-parameter equation, the velocity gap disappears, and the transition line corresponds to $V=0$.

We represent the solution for the order parameter in the form

$$\rho(x, z, t) = \rho(x + Vt, z). \quad (A1)$$

Substituting the ansatz (A1) in Eq. (14) one obtains

$$V\rho_x = \nabla^2 \rho - \rho(1 - \rho)(\delta - \rho). \quad (A2)$$

For $V=0$ Eq. (A2) is reduced to

$$\nabla^2 \rho - \rho(1 - \rho)(\delta - \rho) = 0. \quad (A3)$$

The solution to Eq. (A3) exists only for some specific value of $\delta = \delta_0$ for each h_0 . This value can be obtained from the solvability condition. Since $\partial_x \rho_0$ is the solution of the linearized problem, the solvability condition is obtained with respect to this solution. Multiplying Eq. (A3) by $\partial_x \rho_0$ and performing integration over x and z , one obtains

$$\int_{-\infty}^{\infty} dx \int_{-h}^0 dz \partial_x \rho_0 [\nabla^2 \rho_0 - \rho_0(1 - \rho_0)(\delta_0 - \rho_0)] = 0. \quad (A4)$$

Using integration by parts, we derive

$$\int_{-\infty}^{\infty} dx \int_{-h}^0 dz \frac{\partial}{\partial x} \left((\partial_z \rho_0)^2 + \frac{1}{2} \rho_0^4 - \frac{2}{3} (\delta_0 + 1) \rho_0^3 + \delta \rho_0^2 \right) = 0, \quad (\text{A5})$$

which leads to

$$\left. \int_{-h}^0 dz \left((\partial_z \rho_0)^2 + \frac{1}{2} \rho_0^4 - \frac{2}{3} (\delta_0 + 1) \rho_0^3 + \delta \rho_0^2 \right) \right|_{x=\infty} - \frac{h_0(2\delta-1)}{6} = 0. \quad (\text{A6})$$

For $x \rightarrow \infty$ the solution ρ_0 converges to a pure one-dimensional solution with the first integral

$$-(\partial_z \rho_0)^2 + \frac{1}{2} \rho_0^4 - \frac{2}{3} (\delta_0 + 1) \rho_0^3 + \delta \rho_0^2 = C = \text{const}, \quad (\text{A7})$$

where $C = \frac{1}{2} \rho_0^4 - \frac{2}{3} (\delta_0 + 1) \rho_0^3 + \delta \rho_0^2$ at $z=0$. Therefore, the expression (A6) can be brought to the form

$$2 \int_{-h}^0 dz \left(\frac{1}{2} \rho_0^4 - \frac{2}{3} (\delta_0 + 1) \rho_0^3 + \delta \rho_0^2 \right) \Big|_{x=\infty} - Ch - \frac{h_0(2\delta-1)}{6} = 0. \quad (\text{A8})$$

Setting $h = h_0$ and solving Eq. (A8) for each h , one finds the dependence δ_0 vs h_0 . This dependence is shown in Fig. 11, dotted line. The infinite viscosity limit gives the lower bound of uphill avalanches; however, as one sees in the figure, this limit is rather close to the experimental data.

For $h \gg 1$ one can derive an estimate for h vs δ . In this limit, the solution is given by the front solution Eq. (34). Since for $\delta > 1/2$ the fluidized state invades the solid state, the front travels toward the bottom and stops at the distance $\Delta z \sim \ln(\delta - 1/2) \sim O(1)$ from the bottom. Thus, for $h \gg 1$ one obtains from Eq. (A8) (taking into account $C \rightarrow 0$),

$$h \sim \frac{\ln(\delta - 1/2)}{\delta - 1/2}. \quad (\text{A9})$$

Let us now consider the case $h \sim O(1)$. In this case the transition line $h(\delta)$ can be obtained analytically from the single-mode approximation Eq. (24). To demonstrate that, we first find the position of the line $V=0$ in the (δ, h) plane for $\alpha \rightarrow 0$. Equation (24) has a stationary front solution connecting two outer fixed points A_1 and A_3 of Eq. (24) if its free energy is symmetric, i.e., the roots $A_{1,2,3}$ of equation $\lambda(h)A + [8(2 - \delta)/3\pi]A^2 - \frac{3}{4}A^3 = 0$ satisfy the symmetry condition $A_1 = 0, A_3 = 2A_2$. It gives rise to the expression

$$\delta - 1 - \frac{\pi^2}{4h^2} + \frac{2}{3} \left(\frac{16}{9\pi} (2 - \delta) \right)^2 = 0. \quad (\text{A10})$$

From Eq. (A10) we obtain

$$h = \frac{\pi}{2} \frac{1}{\sqrt{\delta - 1 + \frac{2}{3} \left[\frac{16}{9\pi} (2 - \delta) \right]^2}}. \quad (\text{A11})$$

The dependence $h(\delta)$ agrees with the corresponding dependence obtained from the analysis of the full Eq. (14) [see Eq. (A8)] with a line thickness up to $\delta \approx 0.6$. Also, along this line there is an exact expression for the front solution

$$A_0 = A_\infty [1 + \tanh(\sqrt{3/8} A_\infty x)], \quad (\text{A12})$$

where A_∞ is given by Eq. (27).

APPENDIX B: UPHILL FRONT VELOCITY IN THE LARGE VISCOSITY LIMIT

For finite α we look for the solution in the form

$$A = A_0(x) + \epsilon A_1,$$

$$h = h_0 + \epsilon h_1(x),$$

$$V = \epsilon V_1,$$

$$\delta = \delta^* + \epsilon \delta_1 - \beta \epsilon \partial_x h_1, \quad (\text{B1})$$

where $\epsilon = \sqrt{\alpha}$ and $A_0(x)$ is given by Eq. (A12). Substituting the ansatz (B1) into Eqs. (24) and (25), we obtain in the first order in ϵ ,

$$\hat{L}A_1 = V_1 A_1' - \beta h_1' \left(\frac{8}{3\pi} A_0^2 - A_0 \right) - \frac{\pi^2 A_0}{2h_0^3} h_1 - \delta_1 \left(A_0 - \frac{8}{3\pi} A_0^2 \right), \quad (\text{B2})$$

$$V_1 h_1 = -h_0^3 A_0, \quad (\text{B3})$$

where \hat{L} linearizes Eq. (24) in the vicinity of A_0 at $h = h_0, \delta = \delta^*$.

Equation (B2) has a bounded solution if the right-hand side of Eq. (B2) with h_1 expressed from Eq. (B3) is orthogonal to the zero eigenmode $A_1 = \partial_x A_0$. This solvability condition yields

$$V_1 a_1 + \frac{a_2}{V_1} - \delta_1 a_3 = 0, \quad (\text{B4})$$

where

$$a_1 = \int_{-\infty}^{\infty} (\partial_x A_0)^2 dx = \sqrt{2/3} A_\infty^3, \quad (B5)$$

$$a_3 = \int_{-\infty}^{\infty} \left(A_0 - \frac{8}{3\pi} A_0^2 \right) \partial_x A_0 = 2A_\infty^2 - \frac{64}{9\pi} A_\infty^3.$$

$$a_2 = \int_{-\infty}^{\infty} \left[\beta h_0^3 (\partial_x A_0)^2 \left(\frac{8}{3\pi} A_0^2 - A_0 \right) + \pi^2 / 2 A_0^2 \partial_x A_0 \right] dx$$

$$= A_\infty^3 \left(\frac{4\pi^2}{3} + \frac{16\beta\sqrt{6}h_0^3 A_\infty^2}{15\pi} - \frac{\beta\sqrt{6}h_0^3 A_\infty}{3} \right),$$

Returning to the original notation, we obtain from Eq. (B4)

$$V^2 - \bar{\delta} d_1 V + \alpha d_2 = 0, \quad (B6)$$

with $d_1 = a_3/a_1$, $d_2 = a_2/a_1$, and $\bar{\delta} = \delta - \delta^*$.

-
- [1] H. M. Jaeger, S. R. Nagel, and R. P. Behringer, *Phys. Today* **49** (4), 32 (1996); *Rev. Mod. Phys.* **68**, 1259 (1996).
- [2] L. Kadanoff, *Rev. Mod. Phys.* **71**, 435 (1999).
- [3] P. G. de Gennes, *Rev. Mod. Phys.* **71**, S374 (1999).
- [4] R. M. Nedderman, *Statics and Kinematics of Granular Materials* (Cambridge University Press, Cambridge, England, 1992).
- [5] D. Ertas, G. S. Grest, T. C. Halsey, D. Levine, and L. Silbert, *Europhys. Lett.* **56**, 214 (2001); L. E. Silbert, D. Ertas, G. S. Grest, T. C. Halsey, D. Levine, and S. J. Plimpton, *Phys. Rev. E* **64**, 051302 (2001).
- [6] O. R. Walton, *Mech. Mater.* **16**, 239 (1993); T. Pöshel, *J. Phys. II* **3**, 27 (1993); X. M. Zheng and J. M. Hill, *Powder Technol.* **86**, 219 (1996); O. Pouliquen and N. Renaut, *J. Phys. II* **6**, 923 (1993).
- [7] P. G. de Gennes, in *Powders & Grains*, edited by R. Behringer and Jenkins (Balkema, Rotterdam, 1997), p. 3.
- [8] A. Aradian, E. Raphaël, and P.-G. de Gennes, e-print cond-mat/0112227.
- [9] J.-Ph. Bouchaud, M. E. Cates, J. Ravi Prakash, and S. F. Edwards, *J. Phys. I* **4**, 1383 (1994); *Phys. Rev. Lett.* **74**, 1982 (1995).
- [10] T. Boutreux, E. Raphaël, and P. G. de Gennes, *Phys. Rev. E* **58**, 4692 (1998).
- [11] T. Boutreux and E. Raphaël, *Phys. Rev. E* **58**, 7645 (1998).
- [12] A. Aradian, E. Raphaël, and P.-G. de Gennes, *Phys. Rev. E* **60**, 2009 (1999).
- [13] I. S. Aranson and L. S. Tsimring, *Phys. Rev. E* **64**, 020301(R) (2001).
- [14] L. D. Landau and E. M. Lifshitz, *Statistical Physics* (Pergamon Press, New York, 1980).
- [15] S. F. Edwards and R. B. S. Oakeshott, *Physica A* **157**, 1080 (1989); S. F. Edwards and D. V. Grinev, *Chaos* **9**, 551 (1999).
- [16] R. A. Bagnold, *Proc. R. Soc. London, Ser. A* **225**, 49 (1954); **295**, 219 (1966).
- [17] T. G. Drake, *J. Geophys. Res.* **95**, 8681 (1990).
- [18] J. Rajchenbach, in *Physics of Dry Granular Media*, edited by H. Hermann, J.-P. Hovi, and S. Luding (Kluwer, Dordrecht, 1998), p. 421.
- [19] J. Rajchenbach, *Phys. Rev. Lett.* **88**, 014301 (2002).
- [20] A. Daerr and S. Douady, *Nature (London)* **399**, 241 (1999).
- [21] A. Daerr, *Phys. Fluids* **13**, 2115 (2001).
- [22] O. Pouliquen, *Phys. Fluids* **11**, 542 (1999).
- [23] D. W. Howell, R. P. Behringer, and C. Veje, *Phys. Rev. Lett.* **82**, 5241 (1999).
- [24] D. M. Mueth, G. F. Debregeas, G. S. Karczmar, P. J. Eng, S. R. Nagel, and H. M. Jaeger, *Nature (London)* **406**, 385 (2000).
- [25] S. Nasuno, A. Kudrolli, A. Bak, and J. P. Gollub, *Phys. Rev. E* **58**, 2161 (1998).
- [26] W. Losert, L. Bocquet, T. C. Lubensky, and J. Gollub, *Phys. Rev. Lett.* **85**, 1428 (2000); L. Bocquet, W. Losert, D. Schalk, T. C. Lubensky, and J. P. Gollub, *Phys. Rev. E* **65**, 011307 (2002).
- [27] T. S. Komatsu, S. Inagaki, N. Makagawa, and S. Nasuno, *Phys. Rev. Lett.* **86**, 1757 (2001).
- [28] P.-A. Lemieux and D. J. Durian, *Phys. Rev. Lett.* **85**, 4273 (2000).
- [29] In fact, diagonal elements of the stress tensor should also have a certain dependence on ρ as well. Indeed, presumably they should all become equal to the hydrodynamic pressure in a completely fluidized state. However, we will ignore this complication in this paper.
- [30] E. Cantelaube and J.D. Goddard, in *Powders & Grains* (Ref. [7]), p. 231; O. Narayan and S. R. Nagel, *Physica A* **264**, 75 (1999).
- [31] J. P. Wittmer, M. E. Cates, and P. J. Claudine, *J. Phys. II* **7**, 39 (1997); L. Vanel, Ph. Claudin, J.-Ph. Bouchaud, M. E. Cates, E. Clément, and J. P. Wittmer, *Phys. Rev. Lett.* **84**, 1439 (2000).
- [32] M. E. Cates, J. P. Wittmer, J.-Ph. Bouchaud, and Ph. Claudin, *Phys. Rev. Lett.* **81**, 1841 (1998).
- [33] I. S. Aranson, V. A. Kalatsky, and V. M. Vinokur, *Phys. Rev. Lett.* **85**, 118 (2000).
- [34] J. Rajchenbach, *Adv. Phys.* **49**, 229 (2000).
- [35] S. Nasuno (private communication).
- [36] J.-Ph. Bouchaud and M. E. Cates, *Granular Matter* **1**, 101 (1998).
- [37] G. C. Barker and A. Mehta, *Phys. Rev. E* **61**, 6765 (2000).
- [38] O. Zik, D. Levine, S. G. Lipson, S. Shtrikman, and J. Stavans, *Phys. Rev. Lett.* **73**, 644 (1994).
- [39] K. Choo, T. C. A. Molteno, and S. W. Morris, *Phys. Rev. Lett.* **79**, 2975 (1997).
- [40] I. S. Aranson and L. S. Tsimring, *Phys. Rev. Lett.* **82**, 4643 (1999).
- [41] I. S. Aranson, L. S. Tsimring, and V. M. Vinokur, *Phys. Rev. E* **60**, 1975 (1999).
- [42] L. Prigozhin and H. Kalman, *Phys. Rev. E* **57**, 2073 (1998).
- [43] H. M. Jaeger, C. Liu, and S. R. Nagel, *Phys. Rev. Lett.* **62**, 40 (1989).

- [44] D. Bonamy, F. Daviaud, and L. Laurent, *Phys. Fluids* **14**, 1666 (2002).
- [45] L. D. Landau and E. M. Lifshitz, *Theory of Elasticity* (Pergamon Press, Oxford, 1964).
- [46] H. Hayakawa, *Phys. Rev. E* **60**, 4500 (1999).
- [47] J. M. Carlson and A. A. Batista, *Phys. Rev. E* **53**, 4153 (1996).
- [48] S. B. Savage and D. J. Jefferey, *J. Fluid Mech.* **110**, 225 (1981).
- [49] J. T. Jenkins and M. W. Richman, *Phys. Fluids* **28**, 3485 (1985).
- [50] P. K. Haff, *J. Fluid Mech.* **134**, 401 (1983).
- [51] K. Sela and I. Goldhirsh, *J. Fluid Mech.* **361**, 41 (1998).
- [52] V. L. Ginzburg and L. D. Landau, *Zh. Eksp. Teor. Fiz* **20**, 1064 (1950).
- [53] L. P. Gorkov and G. M. Eliashberg, *Zh. Eksp. Teor. Fiz.* **54**, 612 (1968) [*Sov. Phys. JETP* **27**, 338 (1968)].